

AD-A184 268 MEASUREMENT OF THE ELECTRON DENSITY AND THE ATTACHMENT RATE COEFFICIENT IN THE 20-30 MHz RANGE OF ULTRASHORT WAVELENGTHS 1/1

MEASUREMENT OF THE ELECTRON DENSITY AND THE ATTACHMENT RATE COEFFICIENT IN THE ILLINOIS UNIT OF URBANO GASEOUS

1/1

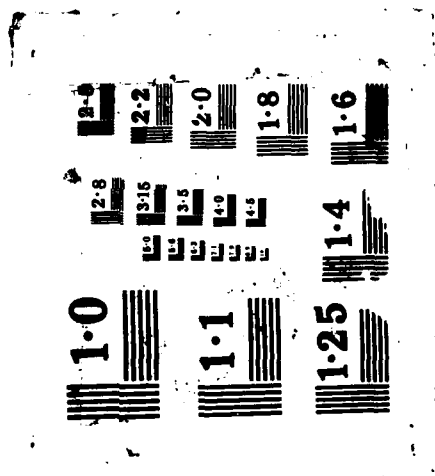
UNCLASSIFIED

AFWAL-TR-86-2031 F33615-83-K-2335

F/G 7/4

NL

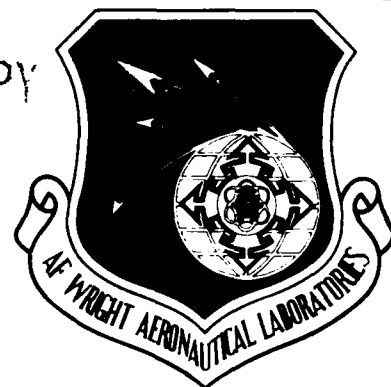
A 10x10 grid of 100 small, dark, rectangular tiles arranged in a larger square pattern. The tiles are separated by thin white lines. The overall image is in grayscale.



AD-A184 268

AFWAL-TR-86-2031

DTIC FILE COPY



MEASUREMENT OF THE ELECTRON DENSITY AND THE ATTACHMENT RATE
COEFFICIENT IN SILANE/HELIUM DISCHARGES

CHARLES B. FLEDDERMAN, J. H. BEBERMAN,
J. T. VERDEYEN

UNIVERSITY OF ILLINOIS
GASEOUS ELECTRONICS LABORATORY
607 E. HEALEY STREET
CHAMPAIGN IL 61820

DTIC
ELECTE
SEP 09 1987
S D

September 1986

FINAL REPORT FOR PERIOD JULY 1983 - MARCH 1986

Approved for public release; distribution is unlimited

AERO PROPULSION LABORATORY
AIR FORCE WRIGHT AERONAUTICAL LABORATORIES
AIR FORCE SYSTEMS COMMAND
WRIGHT-PATTERSON AIR FORCE BASE, OHIO 45433-6563

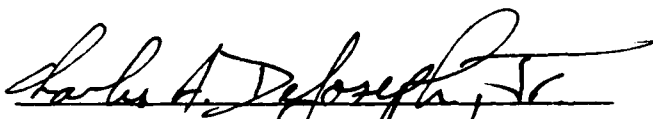
87 9 8 052

NOTICE

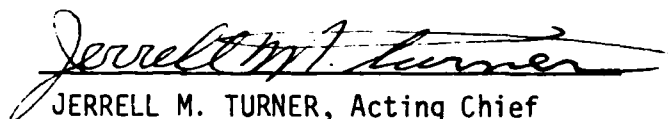
When Government drawings, specifications, or other data are used for any purpose other than in connection with a definitely related Government procurement operation, the United States Government thereby incurs no responsibility nor any obligation whatsoever; and the fact that the government may have formulated, furnished, or in any way supplied the said drawings, specifications, or other data, is not to be regarded by implication or otherwise as in any manner licensing the holder or any other person or corporation, or conveying any rights or permission to manufacture use, or sell any patented invention that may in any way be related thereto.

This report has been reviewed by the Office of Public Affairs (ASD/PA) and is releasable to the National Technical Information Service (NTIS). At NTIS, it will be available to the general public, including foreign nations.

This technical report has been reviewed and is approved for publication.

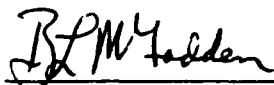


CHARLES A. DEJOSEPH, JR.
Physicist, Power Components Branch
Aerospace Power Division
Aero Propulsion Laboratory



JERRELL M. TURNER, Acting Chief
Power Components Branch
Aerospace Power Division
Aero Propulsion Laboratory

FOR THE COMMANDER



B. L. MCFADDEN, Acting Chief
Aerospace Power Division
Aero Propulsion Laboratory

If your address has changed, if you wish to be removed from our mailing list, or if the addressee is no longer employed by your organization please notify AFWAL/POOC, W-PAFB, OH 45433 to help us maintain a current mailing list.

Copies of this report should not be returned unless return is required by security considerations, contractual obligations, or notice on a specific document.

UNCLASSIFIED

SECURITY CLASSIFICATION OF THIS PAGE

REPORT DOCUMENTATION PAGE

1a. REPORT SECURITY CLASSIFICATION Unclassified		1b. RESTRICTIVE MARKINGS	
2a. SECURITY CLASSIFICATION AUTHORITY		3. DISTRIBUTION/AVAILABILITY OF REPORT Approved for public release; distribution unlimited.	
2b. DECLASSIFICATION/DOWNGRADING SCHEDULE			
4. PERFORMING ORGANIZATION REPORT NUMBER(S)		5. MONITORING ORGANIZATION REPORT NUMBER(S) AFWAL-TR-86-2031	
6a. NAME OF PERFORMING ORGANIZATION University of Illinois	6b. OFFICE SYMBOL (If applicable)	7a. NAME OF MONITORING ORGANIZATION Aeropropulsion Laboratory (AFWAL/POOC) Air Force Wright Aeronautical Laboratories	
6c. ADDRESS (City, State and ZIP Code) Gaseous Electronics Laboratory 607 E. Healey Street, Champaign IL 61820		7b. ADDRESS (City, State and ZIP Code) Air Force Systems Command Wright-Patterson Air Force Base, OH 45433	
8a. NAME OF FUNDING/SPONSORING ORGANIZATION Power Components Branch	8b. OFFICE SYMBOL (If applicable) AFWAL/POOC-3	9. PROCUREMENT INSTRUMENT IDENTIFICATION NUMBER F33615-83-K-2335	
8c. ADDRESS (City, State and ZIP Code) Air Force Wright Aeronautical Laboratory Wright-Patterson AFB OH 45433-6563		10. SOURCE OF FUNDING NOS.	
		PROGRAM ELEMENT NO. 61102F	PROJECT NO. 2301
		TASK NO. S2	WORK UNIT NO. 77
11. TITLE (Include Security Classification) See Reverse			
12. PERSONAL AUTHOR(S) Charles B. Fleddermann, J. H. Beberman, G. Hebner, L. J. Overzet, J. T. Verdeyen			
13a. TYPE OF REPORT Final Tech Report	13b. TIME COVERED FROM 7-12-83 TO 3-30-86	14. DATE OF REPORT (Yr., Mo., Day) September 1986	15. PAGE COUNT 82
16. SUPPLEMENTARY NOTATION			
17. COSATI CODES		18. SUBJECT TERMS (Continue on reverse if necessary and identify by block number)	
FIELD	GROUP		
Plasmas	Discharges Attachment	Attachment in Silane; R.F. Discharges; Modulation	
	RF Discharges	Effects in Deposition	
19. ABSTRACT (Continue on reverse if necessary and identify by block number)			
<p>✓ Discharge processing of semiconductor materials, either as an etch process step in microelectronic fabrication, or as a deposition scheme for solar cell or copier applications, has become indispensable in modern technology. This report is focussed on discharges used for such applications.</p> <p>The thesis by Fleddermann was a basic study of the attachment rate of electrons in discharges involving mixtures of silane and a rare gas as represented by helium. It was found that the primary attaching species was not the silane molecule but some daughter product created by the discharge. These results are indicative of the problems encountered in an attempt to model discharges in such gases: the rates for the radicals may be larger than that of the donor gases.</p>			
20. DISTRIBUTION/AVAILABILITY OF ABSTRACT UNCLASSIFIED/UNLIMITED <input checked="" type="checkbox"/> SAME AS RPT. <input type="checkbox"/> DTIC USERS <input type="checkbox"/>		21. ABSTRACT SECURITY CLASSIFICATION Unclassified	
22a. NAME OF RESPONSIBLE INDIVIDUAL Charles DeJoseph		22b. TELEPHONE NUMBER (Include Area Code) (513)255-2923	22c. OFFICE SYMBOL AFWAL/POOC-3

DD FORM 1473, 83 APR

EDITION OF 1 JAN 73 IS OBSOLETE

UNCLASSIFIED

SECURITY CLASSIFICATION OF THIS PAGE

Item 11. Title

Measurement of the Electron Density and the Attachment Rate Coefficient in Silane/Helium Discharges

Item 19. Abstract

The work also addressed some of the issues associated with modeling parallel-plane RF discharge of the type commonly used in etching and deposition. A simple experiment demonstrates that the central "glow" was actually caused by the ballistic electrons accelerated through the electrode sheath.

Finally, we also document a quite puzzling but unanticipated result using a square-wave modulated RF discharge for the deposition of a-Si:H. It was found that the electron density is enhanced, the deposition rate of a-Si:H changed, of the deposited film reduced by the modulation effect. The detailed physics is not known at this time.

TABLE OF CONTENTS

<u>Section</u>		<u>Page</u>
I	INTRODUCTION	1
II	MEASUREMENT OF THE ELECTRON DENSITY AND THE ATTACHMENT RATE COEFFICIENT IN SILANE/HELIUM DISCHARGES	3
III	MEASUREMENT OF THE ELECTRON DENSITY AND THE ATTACHMENT RATE COEFFICIENT IN SILANE/HELIUM DISCHARGES	67
IV	THE SPATIAL AND TEMPORAL EVOLUTION OF THE FLOW IN A RF DISCHARGE	73
V	ENHANCEMENT OF THE PLASMA DENSITY AND DEPOSITION RATE IN RF DISCHARGES	79



Accession For	
NTIS CRA&I	<input checked="" type="checkbox"/>
DTIC TAB	<input type="checkbox"/>
Unannounced	<input type="checkbox"/>
Justification	
By	
Distribution /	
Availability Codes	
Dist	Avail and/or Special
A-1	

SECTION 1

Introduction

This report describes the work performed under the auspice of USAF contract F33615-83-K-2335 entitled "Studies of the Discharge Effects on Plasma Assisted Deposition of Semiconductor Materials." The main goal was to determine the microscopic plasma parameters in typical discharges used for deposition of semiconductor materials -- in this case hydrogenated amorphous silicon.

One of the biggest problems in such a task is the fact that the discharge creates complex radicals in numbers approaching, if not exceeding, that of the donor molecules (SiH_4). Consequently, modeling of such discharges based upon reaction rates of the donor molecules is less than exact, and even then it is difficult because of the lack of precise transport coefficient. When the radicals are folded into the problem, the difficulties become nigh-onto-unsurmountable at the present time. Consequently, much of our work was aimed at determining the plasma dynamics directly.

This report, then, is divided along the lines of the various approaches taken toward these goals. In Section II, the Ph.D. thesis of C. Fleddermann is presented which discusses the kinetics of the electron density in a hollow cathode discharge in silane helium mixture, which is very similar to that used by those working with proximity discharges. Some of that work is summarized and repeated in Section III, which is the article published in the Journal of Applied Physics. It was also the subject of paper HA-2 presented at the 37th Annual Gaseous Electronics Conference in Boulder, CO, Oct. 9-12, 1984.

Sec. IV deals with the dynamics of an RF glow in the simplest of all rare gases -- helium. Most plasma deposition systems use the planar RF discharge

similar to that studied here. We intentionally avoided the more complex molecular gases so that the complex chemistry of those discharges would not interfere with the plasma problem. That section is a preprint of an article due to be published in the IEEE Transaction of Plasma Science in April 1986. It was also the subject of paper CB-18 presented at the 38th Annual Gaseous Electronics Conference in Monterey, CA, Oct. 15-18, 1985.

Sec. V is a preprint of an article due to appear in the Applied Physics Letters in Mar. 1986. In this paper, we show some rather startling and, as of yet, unexplained plasma dynamics in response to square-wave-modulating the RF excitation of silane-helium mixtures. Conventional wisdoms would suggest that such discharges would reach a quasi-CW state on a time scale of a few hundred microseconds. Much to our surprise, the electron density is enhanced -- even on a time-averaged basis, and the silicon deposition rate is also increased. The physical process for the density enhancement has not been identified, but it appears to occur in discharges in electronegative gases. While the causes have not been identified, it may have the practical application of achieving an enhanced process (i.e., deposition or etching) while minimizing damage to the semiconductor.

SECTION II

MEASUREMENT OF THE ELECTRON DENSITY AND THE ATTACHMENT
RATE COEFFICIENT IN SILANE/HELIUM DISCHARGES

by

Charles Byrns Fledderman

June 1985

TABLE OF CONTENTS

	PAGE
I. INTRODUCTION	1
II. FILM STUDIES	11
III. THEORY OF PLASMA MEASUREMENTS	23
IV. DC MEASUREMENTS	32
V. PULSED MEASUREMENTS	44
VI. SUMMARY AND CONCLUSIONS	57
REFERENCES	59

I. INTRODUCTION

The application of gas discharge technology to problems in the semiconductor industry has revolutionized the processing of semiconductors, contributing in both the areas of etching and deposition of semiconductor materials. Plasma etching (also known as dry etching) of silicon using fluorine bearing gases has made it possible to build microelectronic circuits with device dimensions far smaller than is feasible with conventional wet-etch techniques, and is now an extensively used integrated circuit processing technique in industry.¹ Deposition of semiconductors using plasma techniques is not as well developed a technology, although deposition of nitrides for integrated circuits has been common for some time.²⁻⁴ Deposition from a plasma allows processing at far lower temperatures than can be achieved using pyrolytic methods (preventing diffusion of dopants), promotes chemical reactions that otherwise would not take place, and can even allow the growth of materials that cannot be produced any other way, making the gas discharge a very powerful tool in the production of semiconductors.

One plasma deposited material that is becoming increasingly important is amorphous silicon. Indeed, to date, most electronically useful amorphous semiconductors have been produced by glow discharge deposition techniques. Amorphous materials have traditionally been prepared by quenching from the melt, evaporation or sputtering. These techniques have proven to be inadequate for growing amorphous

semiconductors, since the material produced contains a very high density of unsatisfied "dangling" bonds which cause a very high density of states in the band gap. The high density of states pins the Fermi level near the center of the band gap, precluding doping and the fabrication of useful devices in amorphous silicon. This situation changed in 1969 when amorphous silicon was first deposited at low temperature from a gas discharge in silane, a silicon bearing gas.⁵ During the deposition, significant amounts of hydrogen were incorporated into the film, saturating the dangling bonds, reducing the density of states in the band gap, and providing material that is suitable for electronic applications. In 1975 the first selective doping of amorphous semiconductors was demonstrated,⁶ thus proving the suitability of amorphous silicon for device fabrication. Since that time, a great deal of research has gone into understanding the properties of amorphous silicon, and many uses for amorphous silicon have been proposed. Chief among these uses is in the field of solar photovoltaics. Since amorphous silicon is a disordered solid, the k conservation rules are relaxed, making amorphous silicon a "pseudo-direct" band gap material, having a much higher absorption coefficient for the solar spectrum than does crystalline silicon. The difference in absorption coefficient is illustrated in Fig. 1 where it can be seen that the absorption coefficient for amorphous silicon is about an order of magnitude higher than that for crystalline silicon. Although the electrical properties of amorphous silicon are not as good as those for crystalline silicon, for solar cell applications this is more than made up for by the better optical absorption and greatly reduced production costs of amorphous

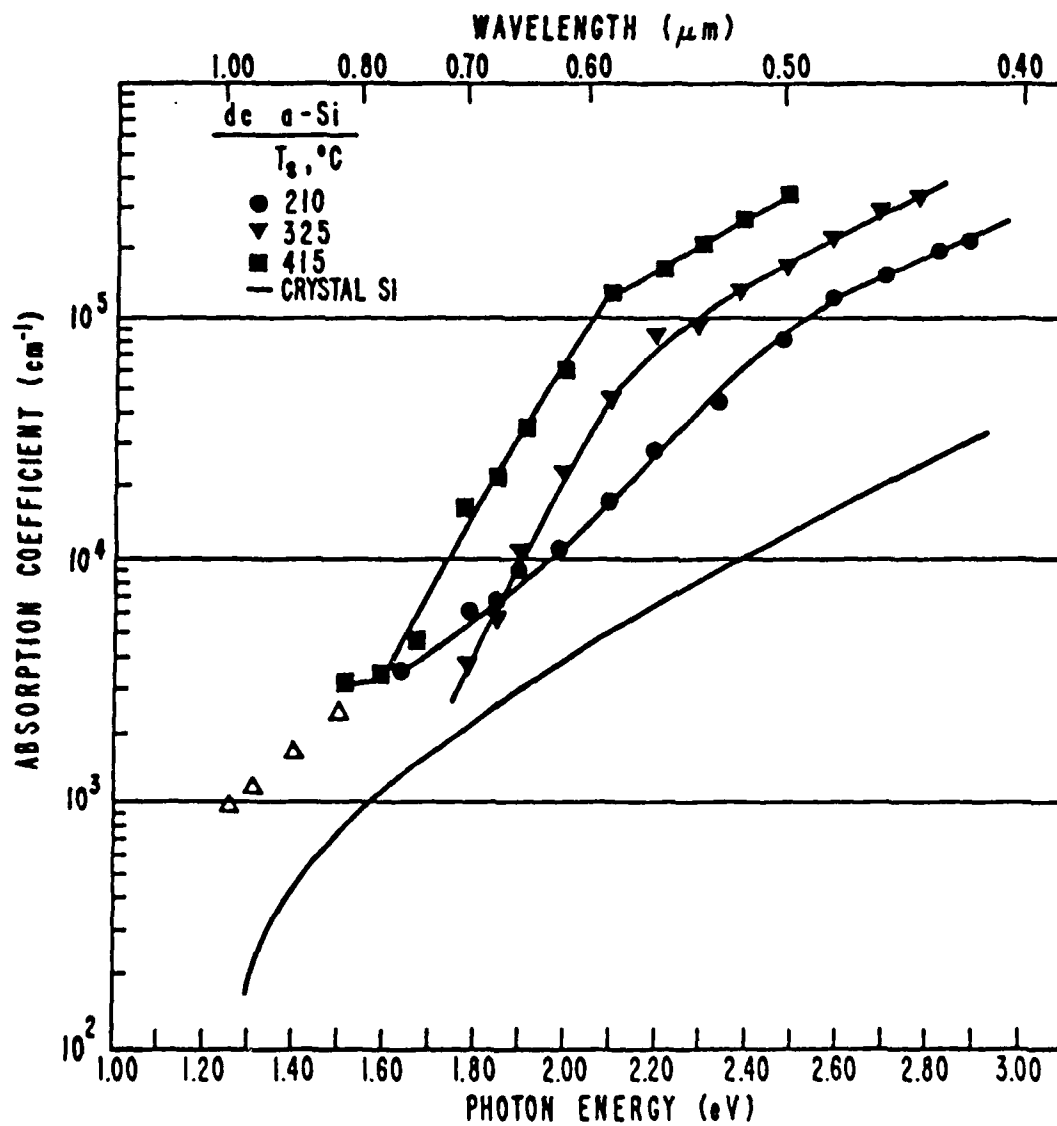


Fig. 1 Absorption coefficient for amorphous and crystalline silicon.
(From ref. 5)

materials.⁸ The highest efficiency achieved for these devices is around 10%⁹ (compared to approximately 18% in single crystal silicon cells)¹⁰ and they have already found commercial application in powering digital watches and calculators. Other potential applications for amorphous semiconductors include photoreceptors, Xerography, FET drivers for large area liquid crystal displays,^{11,12} and devices where radiation damage can degrade crystalline semiconductor performance¹³ (amorphous materials being already disordered, show negligible effects from exposure to radiation). There has also been some interest in using amorphous semiconductor alloys in semiconductor superlattice studies.¹⁴

Of great importance to the commercial future of amorphous semiconductors is an understanding of the deposition process by which they are produced. Although this technology has been around for several years, the deposition process remains more in the realm of art than science. This is partly due to the wide variety of deposition systems in use in various laboratories, including rf (capacitively and inductively coupled) and dc systems. Moreover, even for similar types of deposition systems, there is a great deal of variation from system to system in dimensions, configurations and materials, rendering comparisons between films grown in different laboratories meaningless. The current "state of the art" in deposition is knowing how to set the external parameters (voltage, pressure, gas mixture, etc.) to produce a film of given quality in a given deposition system.

In order to tie together the results obtained in various laboratories and to show what direction needs to be taken to improve the

films that are produced, it is essential to move beyond the macroscopic, external parameters of deposition systems, and try to come to some understanding of the microscopic properties of the deposition plasma itself. This is no easy task, since deposition discharges typically contain many different atomic and molecular neutrals, ions, and excited states. A representative sample of these is found in Table 1. There are also a large number of possible plasma kinetic processes which affect the deposition process, some of which are shown in Table 2. Thus, the deposition plasma is an enormously complex system, the understanding of which involves determining which of the species and processes mentioned in Tables 1 and 2 are important, and how they affect the plasma and the deposition process. Perhaps the most important of the species shown in Table 1 are electrons since electrons fuel so many of the kinetic processes mentioned in Table 2. Therefore, understanding the properties of the electrons in the discharge is a good first step in gaining an understanding of the deposition process.

There have been several previous studies aimed at understanding these microscopic properties of the discharge plasma. Many have studied the properties of the deposited films, measuring surface morphology, hydrogen content and type of bonding, and attempted to correlate these with external discharge parameters to infer some of the plasma characteristics. Typical of these studies is that of Knight et al.,¹⁵ who studied the effect of dilution of silane by noble gases to determine the effects on growth rate, and the effect of the diluent specie on the film structure. Potts et al.¹⁶ studied the effects of gas pressure and rf power on the optical absorbtion and hydrogen content of

Table 1 Species present in a typical silane deposition discharge.

Species present:

Neutrals: He, SiH₄, SiH₃, ..., H₂, H, Si_xH_y (x ≥ 2)

Charged particles: e⁻, He⁺, SiH_x⁺, H⁺, SiH_x⁻

Excited states: He^{*}, SiH_x^{*}, H^{*}

Table 2 A sample of possible plasma kinetic processes (with examples),
for deposition discharges.

Plasma kinetic processes:

Dissociation



Ionization



Recombination



Attachment



Charge Exchange



the films. These types of studies are important in terms of learning how to get films with specific qualities, but at best yield only indirect and incomplete information on the actual deposition process.

More direct measurements of plasma properties that have been performed include mass spectroscopic studies, optical emission measurements, and plasma probe studies. Mass spectroscopic measurements give information on the dissociation process, allow a determination of the presence of various species, and permit an inference of the kinetic processes in the discharge. Drevillon et al.¹⁷ have used a mass spectrometer in a low pressure dc discharge to study the dissociation process and compare films grown from neutrals to those grown from ionic species. Robertson et al.¹⁸ studied the spatial dependence of species concentrations and found that SiH_3 is the predominant radical just above the substrate. Turban and coworkers,^{19,20} Haller,²¹ and Weaklein et al.²² have used quadrupole mass spectroscopic techniques to study the kinetic processes in the plasma and to generate a model of the discharge plasma. Mass spectroscopy suffers from the drawback that it is a perturbative technique, and due to sheaths, etc., there is a difference in what is in the plasma and what winds up going through the quadrupole. These drawbacks are somewhat mitigated by using a different mass spectroscopic method, Fourier Transform Mass Spectroscopy.²³ Haaland²⁴ has applied this technique to dissociation experiments in silane, and is able to find the time dependence of some of the radical species concentrations. This technique is just beginning to be used for deposition plasmas.

Optical emission spectroscopy is a method whereby spontaneous

emission from the plasma is monitored to determine what species are present and what effect changes in external parameters have on the plasma. Kampas et al.²⁵ studied the emission intensities of various species in the discharge as a function of silane percentage and rf voltage. From this they infer the electron density and electron temperature dependence in the plasma, and are able to model the product formation paths. Hirose and coworkers²⁶ and Matsuda et al.²⁷ also monitored various species in the plasma and tried to correlate their relative densities with the hydrogen content of films grown in their systems. This method of studying plasmas is limited by the fact that only some of the constituents of the plasma have known emission spectra. For example, SiH_4 and SiH_3 do not emit line or band spectra, so only an incomplete picture of the plasma is possible with this technique.

There have been attempts to measure the electron density directly in the plasma. Kocian et al.^{28,29} used plasma probe methods to measure electron density and electron temperature in order to get an idea about the relative likelihood of various plasma processes. Gleres and his co-workers³⁰ used the same Langmuir probe techniques and correlated their results with mass spectroscopic measurements of neutrals in the plasma. It is important to measure these parameters; however, Langmuir probes also perturb the plasma, making results difficult to interpret.

This study seeks to increase the understanding of deposition plasmas by utilizing non-perturbative microwave diagnostic techniques to measure the electron density in silane/helium discharge plasmas. From these measurements, a determination of the relative importance of some fundamental kinetic processes can be made. In Chapter 2, the growth

system that was developed for this research is discussed, along with results of some diagnostics on films grown in the system. In Chapter 3, the theory of the microwave measurement technique is described. In Chapter 4, the results of electron density measurements for a dc discharge are presented, followed in Chapter 5 by measurements using a pulsed power supply.

II. FILM STUDIES

The glow discharge growth system used in this study is shown in Fig. 2 in the configuration for film growth. The discharge is initiated in a hollow cathode, which is a 9.8 cm inner diameter stainless steel cylinder, 17.5 cm long. The hollow cathode configuration was chosen for this work because it facilitates certain plasma diagnostics which will be discussed in subsequent chapters, and because it is sustained in a manner similar to that for an rf discharge,³¹ which is the more commonly used plasma deposition system. Thus, results obtained in the hollow cathode should be equally applicable to rf systems. The hollow cathode is connected to a turbo-molecular pump capable of evacuating the system to 10^{-5} Torr or better before experiments, and a fore pump is used while flowing gases. During experiments, helium and 10% silane in helium are introduced into the system through a flow controller which provides reproducible and controlled pressures, flow rates, and flow ratios of gases, and allows the percentage silane in the discharge gas to be continuously varied between 0 and 10%.

Substrates for growth were attached either mechanically or using a high-vacuum compatible adhesive to a stainless steel substrate holder in an arm off the hollow cathode. The distance from the substrate holder to the hollow cathode can be changed from 0 to 10 cm. The hollow cathode and the substrate holder have different power supplies, so the current (and voltage) for the hollow cathode and for the substrate holder can be varied relatively independently of each other. Figure 3 shows the

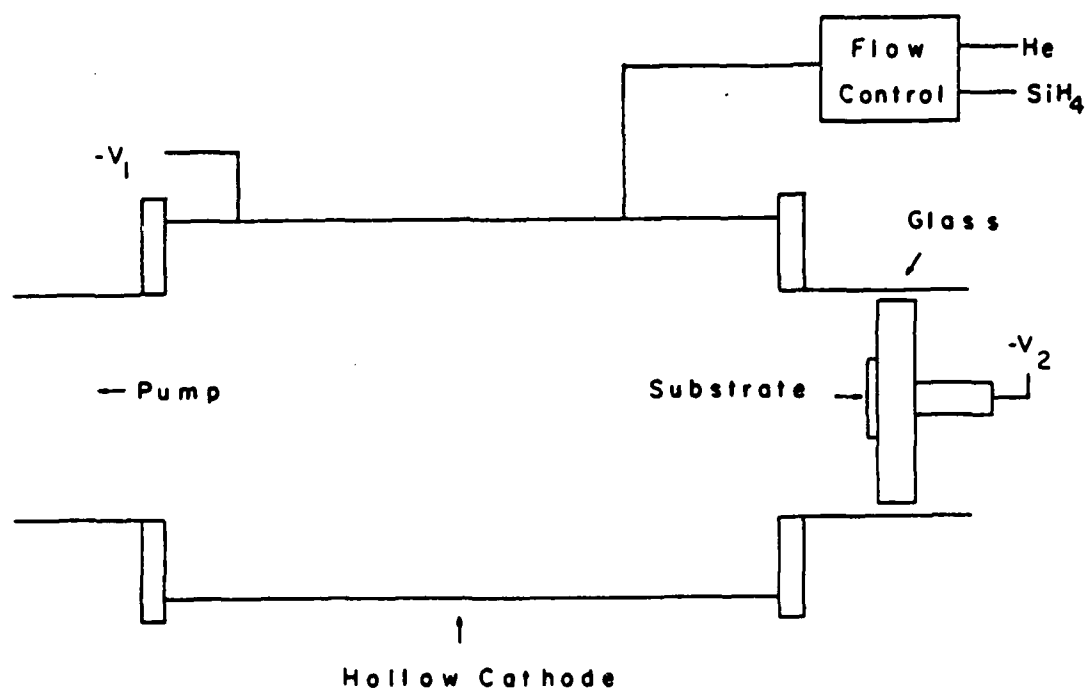


Fig. 2 Hollow cathode discharge system used for growth of amorphous silicon films. (System ground is at pump.)

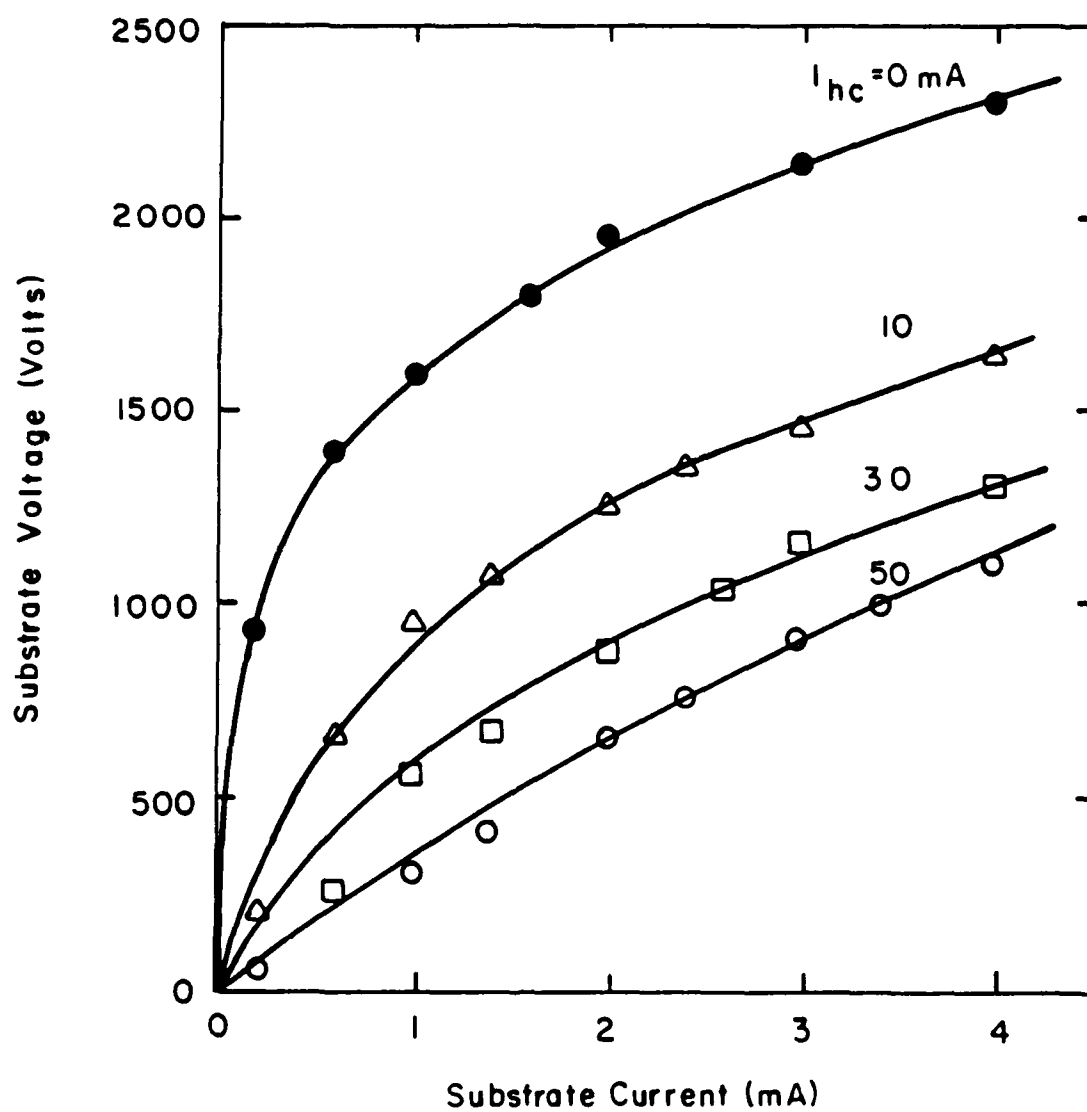


Fig. 3 Current-voltage characteristic of the hollow cathode growth system.

current-voltage characteristic for the discharge growth system, with the substrate voltage as a function of the current to the substrate holder and current in the hollow cathode discharge. For a constant substrate voltage, the current to the substrate is enhanced by an increase in hollow cathode current. The substrates were either glass or crystalline silicon, depending on the type of film measurements to be made.

To determine whether the hollow cathode growth system is similar to the systems used in other laboratories, films were grown and diagnostics performed on them to determine if the properties of the films are comparable to those reported in the literature. In general, the films were brownish in color, adhered well to the substrate when the substrate was biased negatively, were uniform and had a low density of pinholes. When the substrate holder was biased positively, the films were powdery, and easily removed from the substrate. Figure 4 shows the growth rate of the film as a function of current to the substrate holder, which was measured by masking a part of the substrate during the growth, removing the mask, and measuring the step height using a mechanical stylus surface profiling instrument. The growth rates shown in Fig. 4 are for silicon substrates, and are roughly 50% higher than growth rates for glass substrates under the same discharge conditions. The growth rates shown here are well within the range reported in the literature for both rf and dc deposition systems.³²

Raman scattering experiments were performed to determine whether the films were crystalline, polycrystalline, or amorphous. For crystalline silicon, only phonons near the zone center contribute to the Raman scattering; therefore, the spectrum of the scattered radiation is

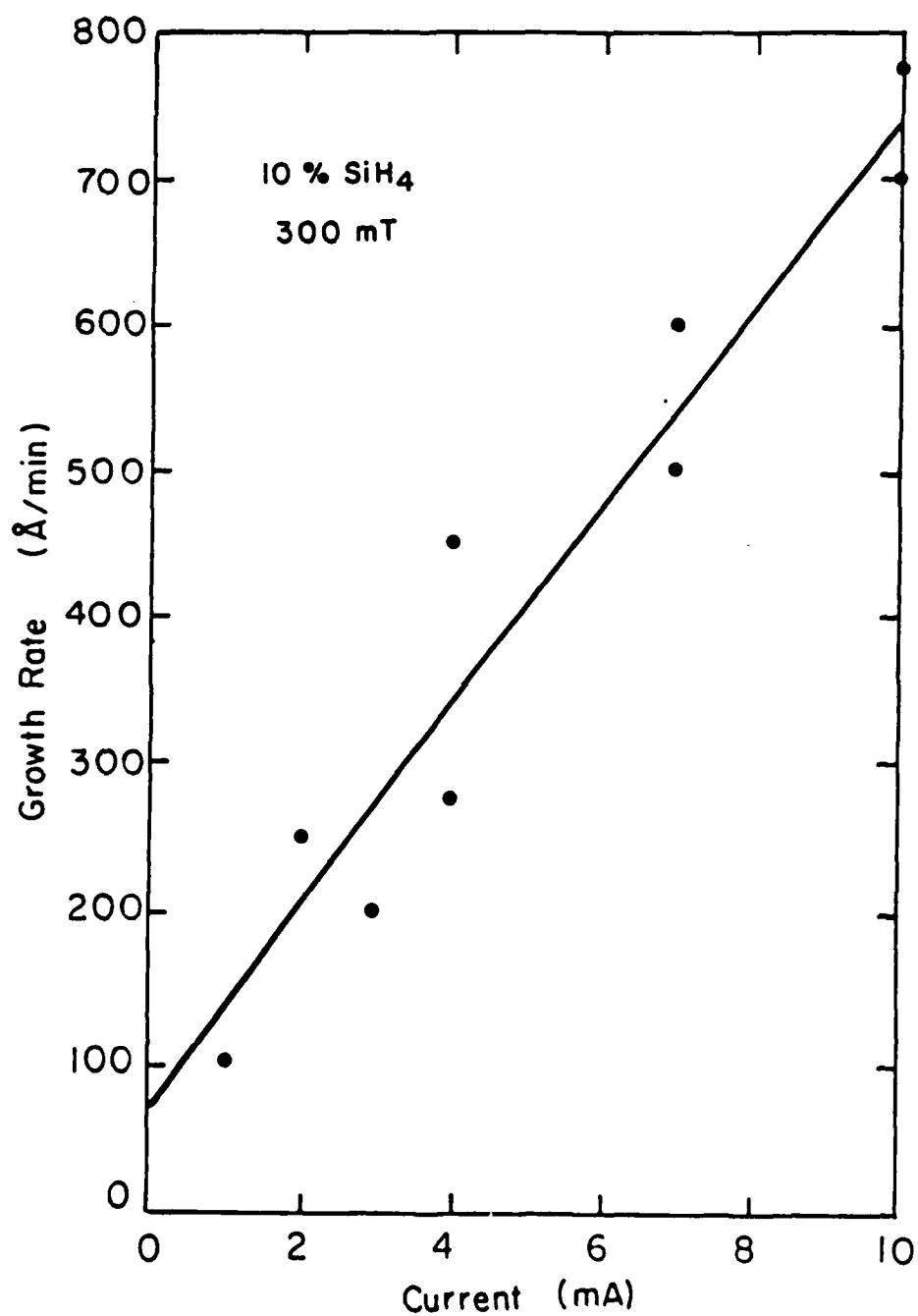


Fig. 4 Growth rate of amorphous silicon as a function of current to the substrate holder.

narrow. In contrast, in amorphous silicon, all vibrational modes can contribute to the scattering, and the spectrum is broad.³³ Thus, Raman experiments give a sensitive measurement of what type of film has been grown. Figure 5 shows the Raman spectrum of a typical film grown in the hollow cathode system. The broad peak around the origin (0 cm^{-1}) is due to Rayleigh scattering from the pump laser. For crystalline silicon, the scattered spectrum should be quite narrow ($\sim 5\text{ cm}^{-1}$) and centered around 520 cm^{-1} .³⁴ For amorphous silicon, the peak is shifted to 480 cm^{-1} and is considerably broadened.³³ In Fig. 5 the spectrum features a very broad ($\sim 100\text{ cm}^{-1}$) peak centered around 480 cm^{-1} , so this film is clearly amorphous. The Raman effect can also give information on impurities in the sample. There is a stretching mode of the Si-H bond at around 2100 cm^{-1} ,^{35,36} which can be seen as a slight, broad bump in Fig. 5. This indicates that there is a small amount of hydrogen present in the film.

The amount of hydrogen contained in the film is a very important parameter since the optical absorption coefficient and the electrical properties of the film are determined to some extent by the bonded hydrogen in the film. Figure 6 shows the absorption coefficient as a function of wavelength for films grown at three different substrate bias currents (and hence three different voltages) near room temperature. A broad-band light source and an optical multi-channel analyzer are used to measure the light transmitted by the glass substrate and that transmitted by both the substrate and film. Ignoring interference effects due to reflections from the film/substrate interface, the expression for the absorption coefficient is given by

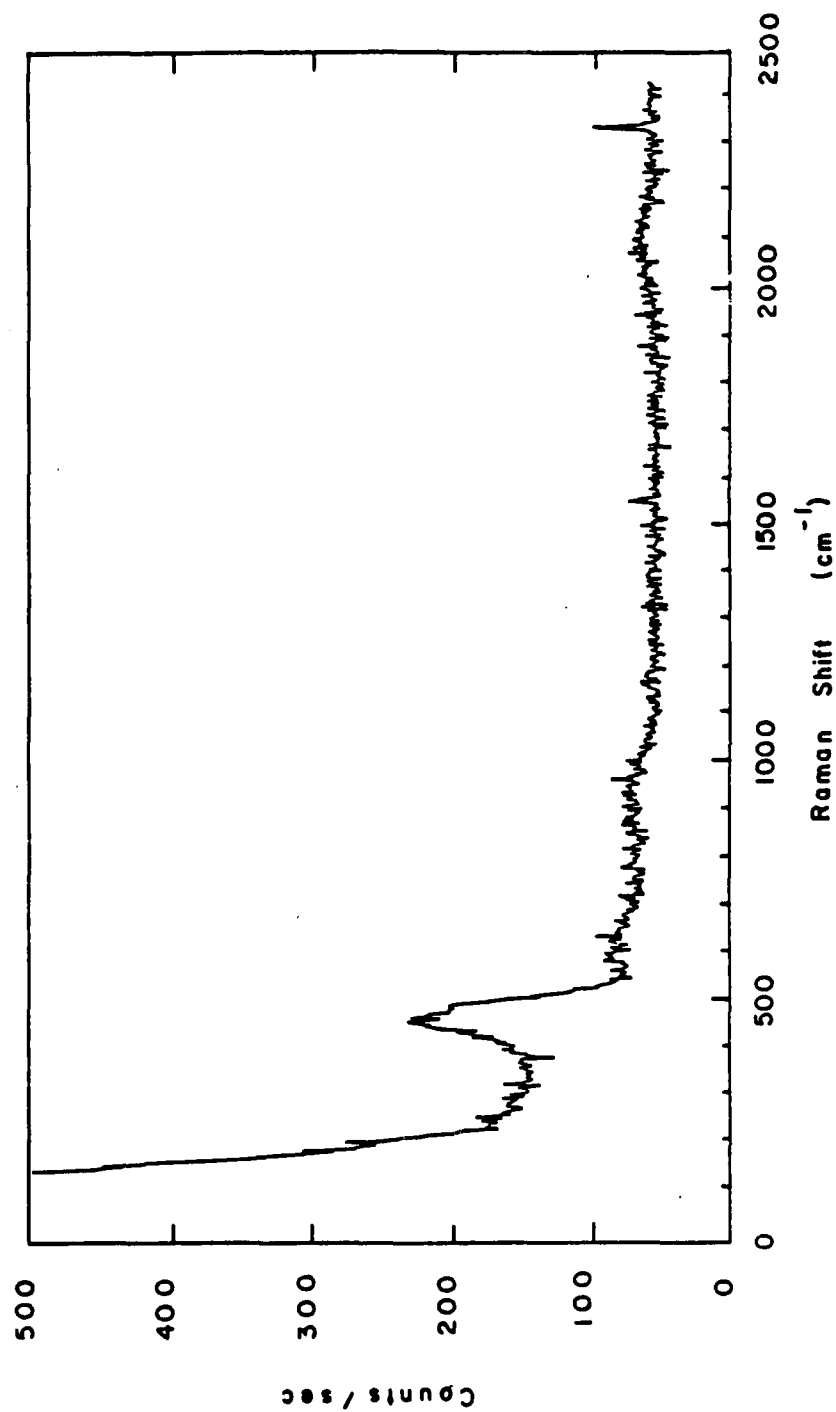


Fig. 5 Raman spectrum of typical film grown in the hollow cathode discharge. (Measurement performed by Dr. P. Hargis of Sandia National Laboratories.)

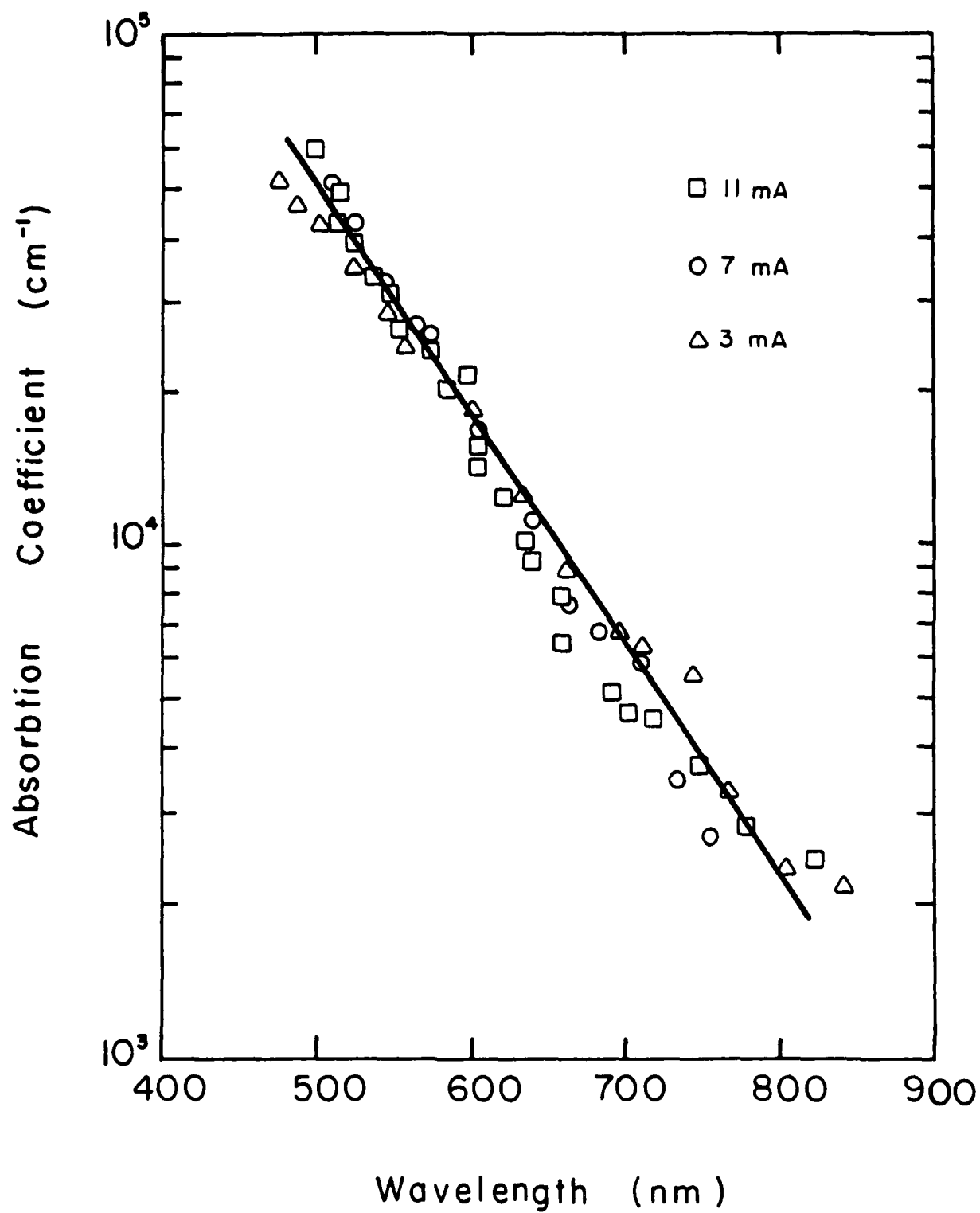


Fig. 6 Absorption coefficient for films grown in apparatus of Fig. 2.

$$\alpha = \frac{1}{t} \ln \frac{I_o}{I_t} \quad (1)$$

where t is the film thickness, I_o is the intensity of light transmitted by the substrate, and I_t is the the light intensity transmitted by the film/substrate combination. In Fig. 6, it can be seen that there is no difference in the absorbtion coefficient of the films grown at different substrate biases. The optical band gap is determined from the absorbtion coefficient data of Fig. 6 using the method outlined by Tauc.³⁷ The square root of the product of the absorbtion coefficient and the photon energy $(\alpha h\nu)^{1/2}$ is plotted against the photon energy $(h\nu)$, and a straight line extrapolated from the higher energy data. The intercept of this line with the energy axis is the optical band gap. A plot of $(\alpha h\nu)^{1/2}$ versus $h\nu$ for the data of Fig. 6 is shown in Fig. 7, giving an optical band gap for the film of approximately 1.75 eV. Figure 8 is a compilation from the literature of the results of various experiments correlating the optical band gap with the hydrogen content of amorphous silicon films.³⁸ From Fig. 8, the atomic percent hydrogen for the films in this study is determined to be 12 percent, which is comparable to the results obtained by Zanzucchi et al.⁷ of 10 atomic percent hydrogen for films grown in a dc proximity discharge at room temperature.

The results of measurements performed on typical films presented in this chapter show that although a rather unique growth system, the dc hollow cathode, was used, the results obtained here are very similar to those reported by other workers using very different growth systems- our

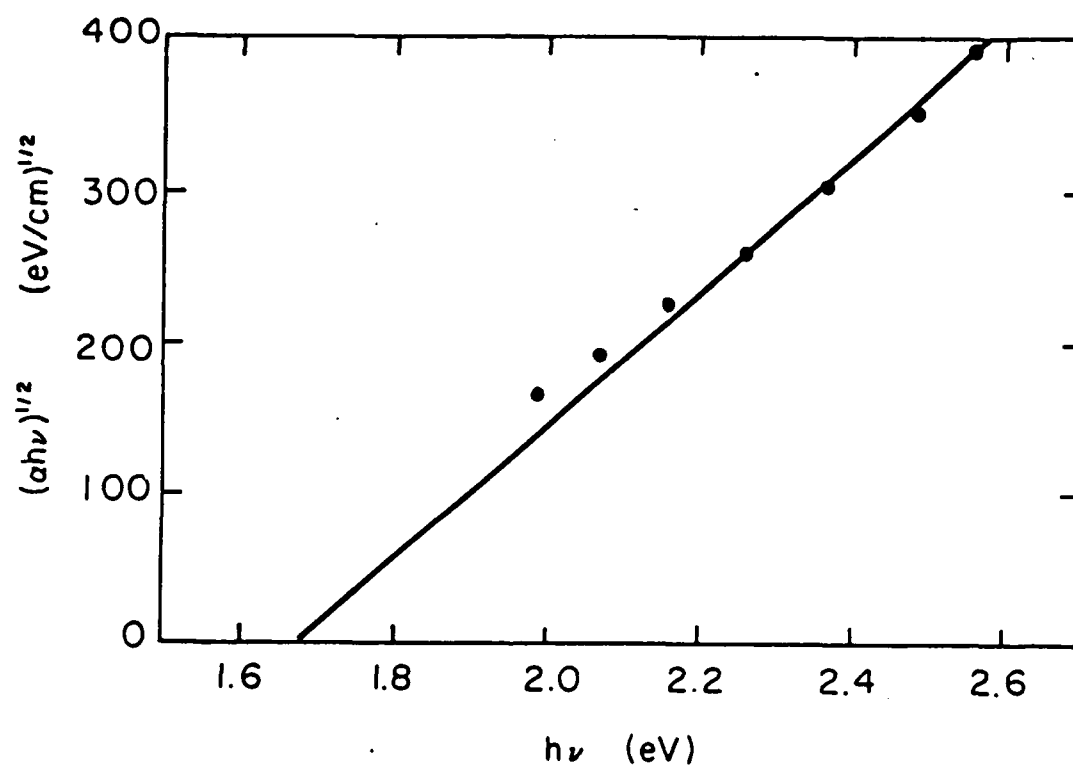


Fig. 7 Determination of the optical bandgap for amorphous films from the absorbtion data of Fig. 6.

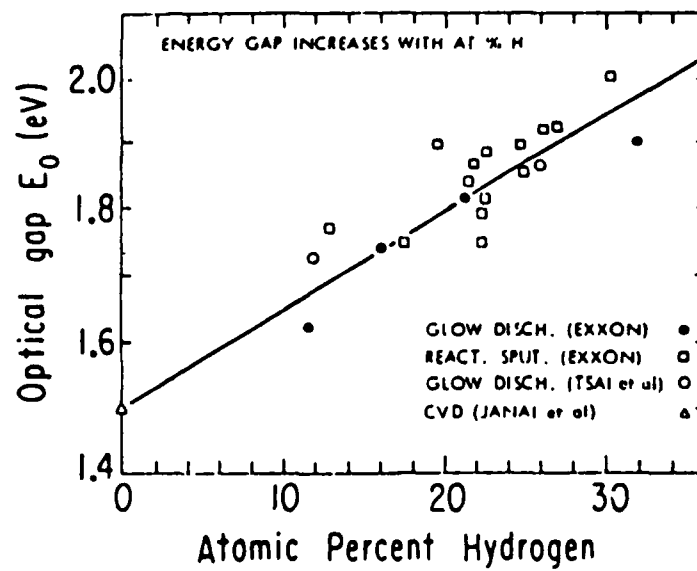
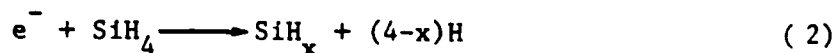


Fig. 8 Dependence of the optical bandgap of amorphous silicon on hydrogen content of the film. (From ref. 38)

films are amorphous with a fairly low hydrogen content. This indicates that the processes taking place in plasmas in deposition systems are fundamentally system independent. Therefore, the results of experiments measuring plasma properties in the hollow cathode system will be applicable to other silane discharge systems as well.

III. THEORY OF PLASMA MEASUREMENTS

The process of deposition of amorphous silicon from a silane plasma is primarily initiated with the dissociation of the parent SiH_4 molecules by electron impact:



This reaction, like many others mentioned in Chapter 1, involves collisions of free electrons with some other constituent in the discharge; thus, the density and energy of free electrons in the plasma are very important parameters. Among other things, the plasma electron density determines the plasma potential, the thickness of the sheaths, and reaction pathways, and is thus an essential component in realistic models of the plasma deposition process.

A sensitive, non-perturbative method for measuring the electron density utilizes the shift in resonant frequency of a microwave cavity when a dielectric (in this case a plasma) is introduced into it. The apparatus used for this measurement is shown in Fig. 9. This is the same system shown in Fig. 2 modified to form a microwave cavity: the substrate holder has been removed, and two stainless steel endplates (with 2.5 cm centered holes to allow gas flow) have been attached to either end of the hollow cathode. The cavity is excited using a loop antenna, and another loop antenna is used to detect the electric field in the cavity. A wavemeter measures the frequency of the energy from the

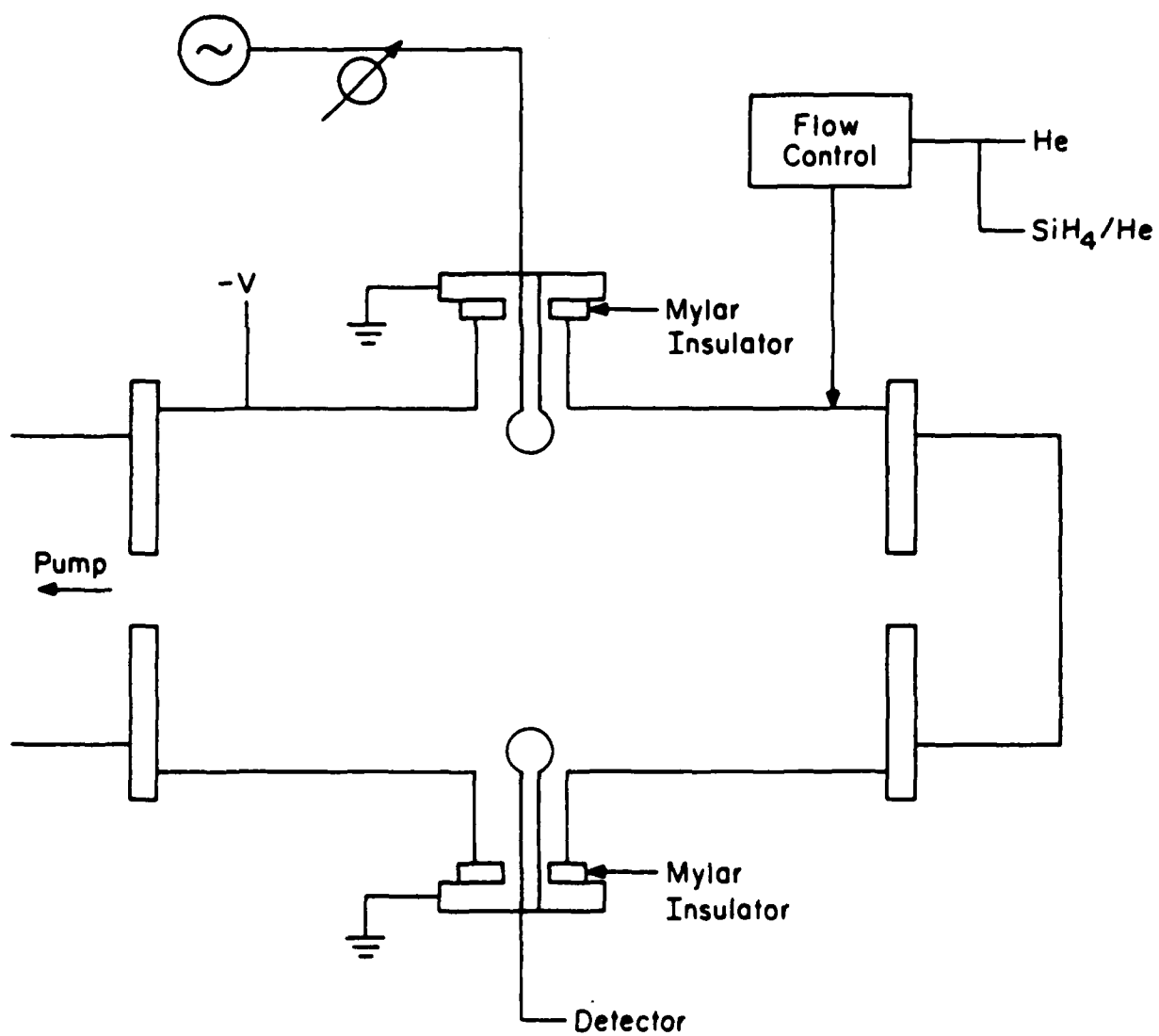


Fig. 9 Experimental apparatus of Fig. 2 modified to measure the plasma electron density.

microwave generator, and a crystal diode is used to detect the signal from the output loop.

The magnitude of the resonant frequency shift of the cavity caused by the introduction of the plasma can be determined using a simple perturbation theory.³⁹ Assuming that for low electron densities the field configuration in the cavity is not significantly altered by the plasma compared to the empty cavity, the shift in resonant frequency for the cavity is

$$\frac{\Delta f_o}{f_o} = \frac{e^2 N_e}{2m\epsilon_o \omega_o^2} \quad (3)$$

where f_o is the resonant frequency, Δf_o is the resonant frequency shift, and N_e is the spatially averaged electron density in the cavity. Equation (3) indicates that the electron density is directly proportional to the shift in resonant frequency of the cavity. The electron density N_e is not spatially uniform, so the average electron density is obtained by weighting N_e by the electric field:

$$N_e = \frac{\int_v N_e E_o^2 dv}{\int_v E_o^2 dv} \quad (4)$$

In order to determine N_e using Equations (3) and (4), the field configuration (E_o) for the resonant mode and the spatial variation of N_e must be known. Since the resonant frequency shift is due to the interaction of free electrons in the plasma with the microwave electric field, measurements of Δf_o for modes with different field

configurations will yield information on the spatial variation of N_e . The microwave generator frequency was swept over a broad range, and two high Q cavity modes were observed. To determine what these two modes were, and thus to determine the associated field configurations, the frequency generator was set to a resonance, a piece of plexiglass inserted into the cavity to perturb the electric field and hence the output signal at the detector, and the perturbations mapped out as a function of r , ϕ , and z . Figure 10 shows the result of these measurements for one of the cavity modes with variations characteristic of the TE_{111} mode. Similarly, Fig. 11 is assigned to the TE_{311} mode. In this cavity, the TE_{111} oscillates at 1.955 GHz and the TE_{311} mode at 4.071 GHz, with cavity Q's of 980 and 580 respectively.

Having identified the resonant modes of the cavity, the electric field configuration for both modes can be readily determined. The electric field components for a TE mode in a cylindrical wave guide are⁴⁰

$$E_z = 0 \quad (5a)$$

$$E_r = \frac{-j\omega\mu n}{h^2 r} C_n J_n(hr) \sin(n\phi) \quad (5b)$$

$$E_\phi = \frac{-j\omega\mu n}{h^2 r} C_n J'_n(hr) \cos(n\phi) \quad (5c)$$

where n is the first digit in the mode number, C_n is a constant, and

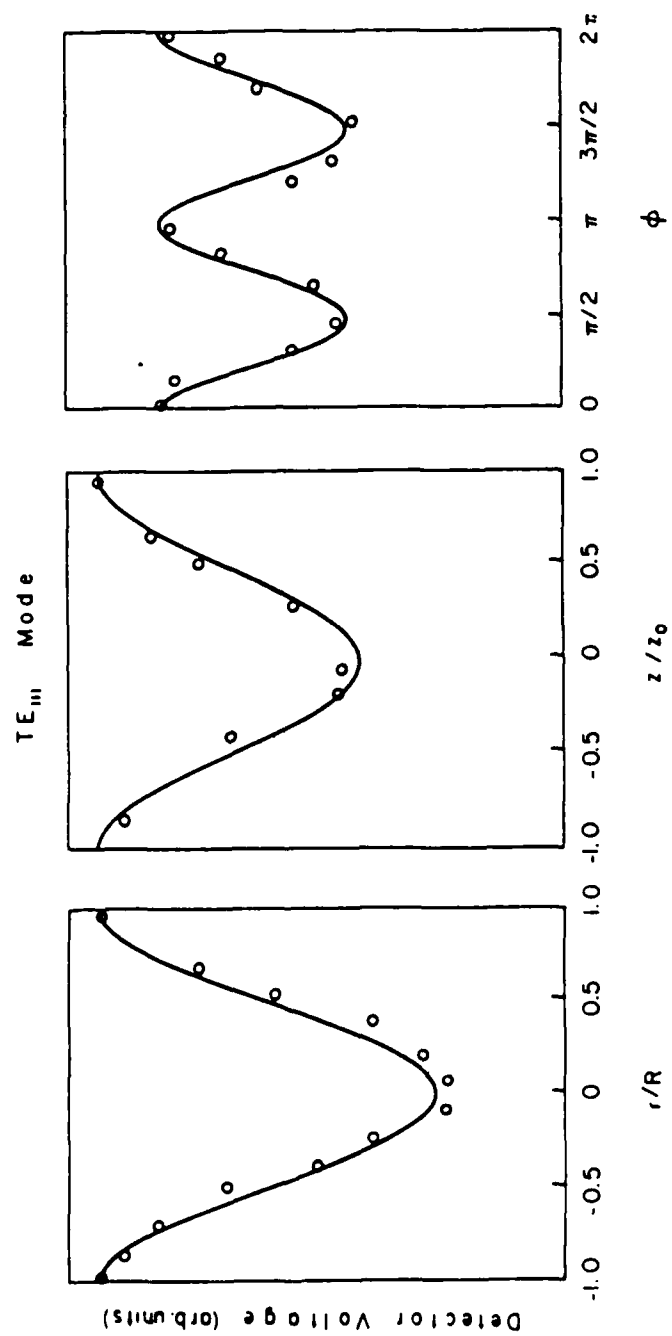


Fig. 10 Cavity field configuration indicating the TE_{111} mode.

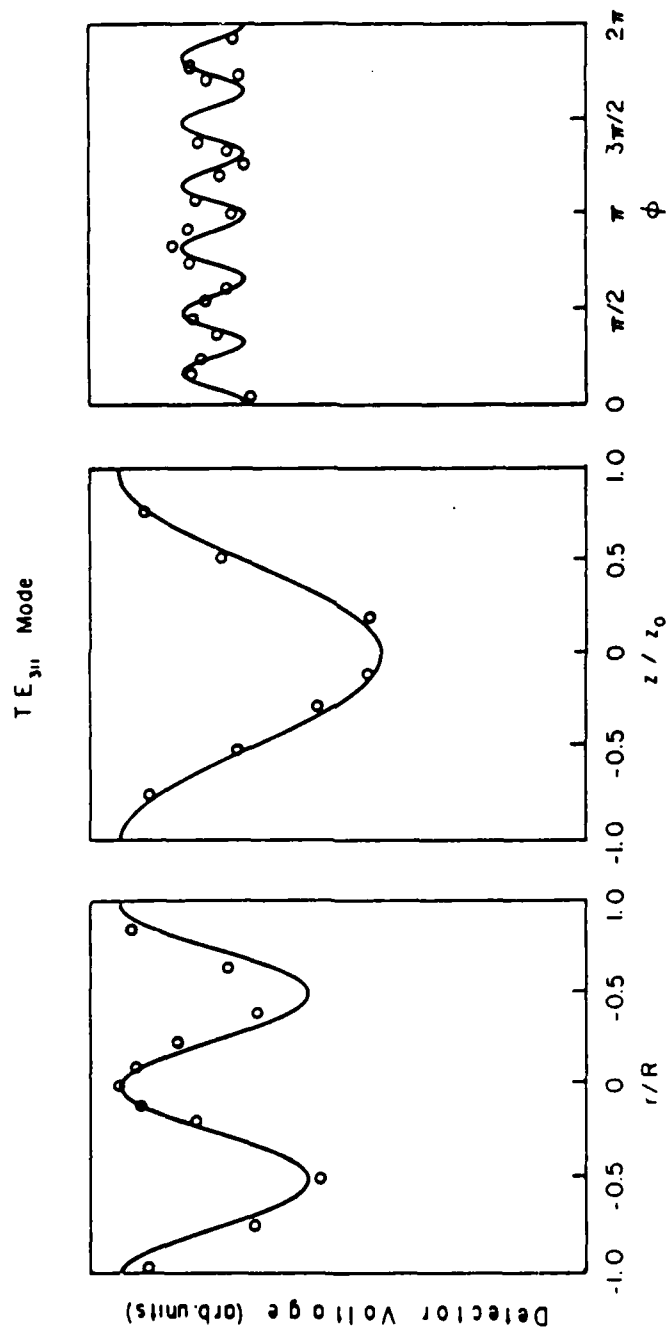


Fig. 11 Cavity field configuration indicating the TE_{311} mode.

J_n is the nth order Bessel function of the first kind. E_o^2 is the sum of the squares of the field components:

$$E_o^2 = E_z^2 + E_r^2 + E_\phi^2 \quad (6)$$

Using the identity

$$J'_n(x) = \frac{1}{2}[J_{n-1}(x) - J_{n+1}(x)] \quad (7)$$

we get

$$E_o^2 = \frac{\omega \mu n}{h^2 r}^2 C_n^2 J_n^2(hr) \sin^2(n\phi) + \frac{\omega \mu n}{h^2 r}^2 C_n^2 \{J_{n-1}(hr) - J_{n+1}(hr)\}^2 \cos^2(n\phi) \quad (8)$$

Equation (8) has been plotted as a function of r for both the TE_{111} mode and the TE_{311} mode in Fig. 12, where it is seen that the electric field distribution for each of the two modes is very different. The TE_{111} mode emphasizes the central core of the electron density distribution, whereas the TE_{311} mode emphasizes the electron density closer to the wall. Hence, measurements of the resonant frequency shift for both modes under the same discharge conditions are complementary, and allow an inference of the spatial variation of the electron density.

The final steps in using Equations (3) and (4) to determine the

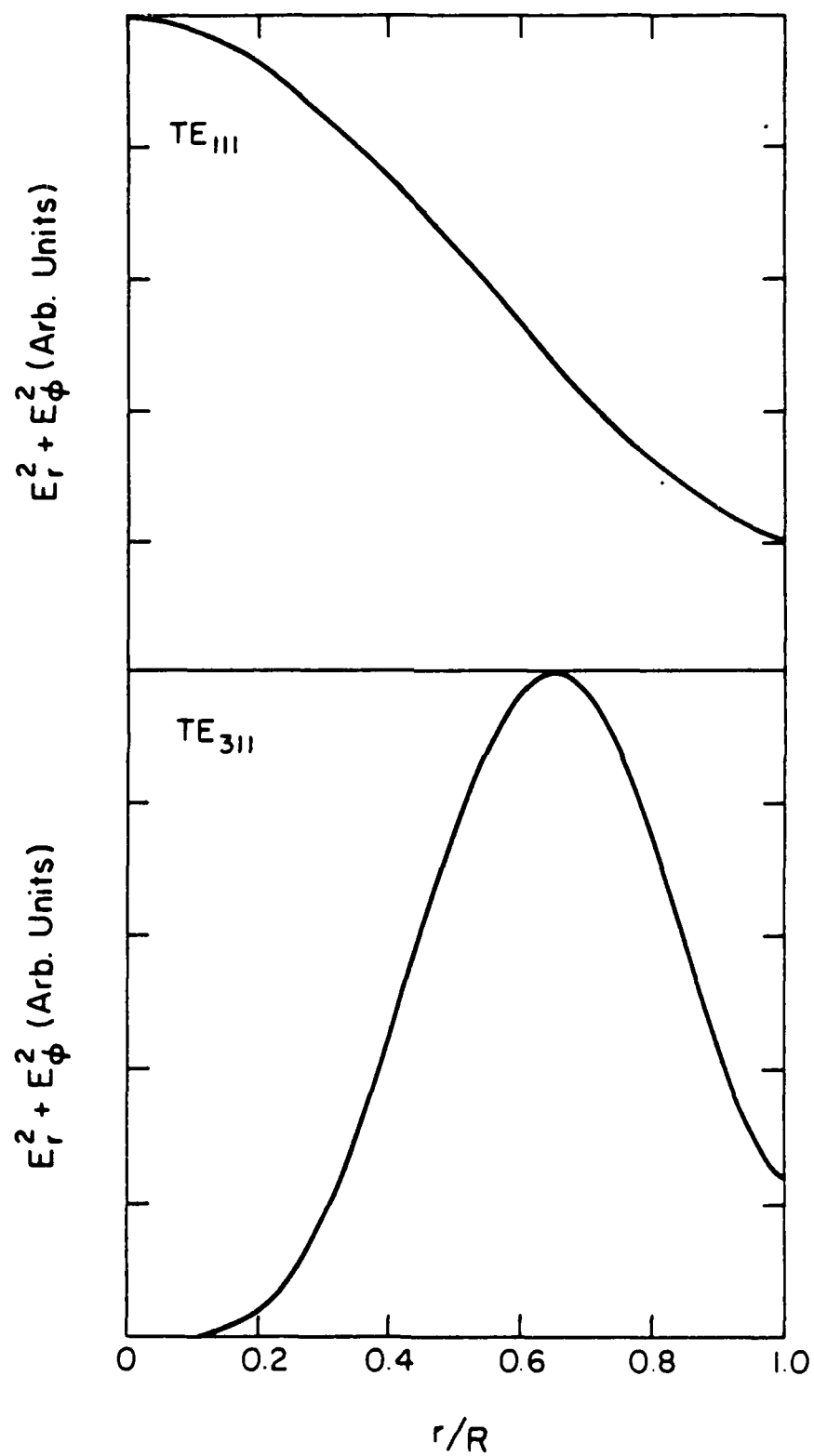


Fig. 12 Radial distribution of the square of the electric field (E_o^2).

electron density are to assume a functional form for the spatial variation of N_e and use the frequency shift data for the two cavity modes to determine the parameters of the functional form. For this study, the electron density was assumed to be of the form:

$$N = N_0 (1 - (r/R)^{2m}) \quad (9)$$

where N_0 is the axial electron density (the density down the axis of the cavity at $r=0$), R is the radius of the cavity, and m is an integer. For this distribution, the electron density is highest at the center of the cavity and drops off to zero at the wall. The value of m determines how rapidly the electron density drops to zero. It is also assumed that the variation of the electron density in the z direction can be ignored since the cavity is long compared with the sheath thickness at the endplates. Using Equations (3), (4), and (9), and the experimental data for the frequency shift for both modes, a computer was used to determine N_0 and m for all discharge conditions.

In this chapter, the theoretical basis and the experimental procedure for measuring the electron density in the hollow cathode/microwave cavity have been discussed. In the following chapters, results of electron density measurements performed in discharges with helium and silane diluted in helium will be presented.

IV. DC MEASUREMENTS

The method outlined in Chapter 3 was used to determine the electron density in the hollow cathode discharge system. The shift in resonant frequency was measured as a function of gas pressure, discharge current and gas mixture for both the TE_{111} and TE_{311} modes. For these experiments, pure helium was used as a baseline with which to compare the results for silane diluted in helium. The resonant frequency of the empty cavity is determined by adjusting the frequency of the microwave generator, observing the peak in the detector signal, and using the wavemeter to determine the frequency. The procedure is identical when there is a plasma in the cavity, except that as the electron density increases, the cavity Q decreases, which makes the frequency more difficult to determine.

Typical data for these measurements are shown in Fig. 13, a plot of the shift in resonant frequency of the cavity for both modes as a function of hollow cathode current for a 1% SiH_4 in helium mixture at 300 mT. As expected, increasing the discharge current increases the electron density due to increased ionization in the plasma. Also, the magnitude of the frequency shift is much smaller for the TE_{311} mode than for the TE_{111} mode, which indicates that for these discharge conditions, the electron density is much higher in the center of the cavity than towards the wall. More will be said about this later.

Data such as that in Fig. 13 are analyzed, as discussed in Chapter 3, using a computer to calculate the values for N_0 and m in Equation

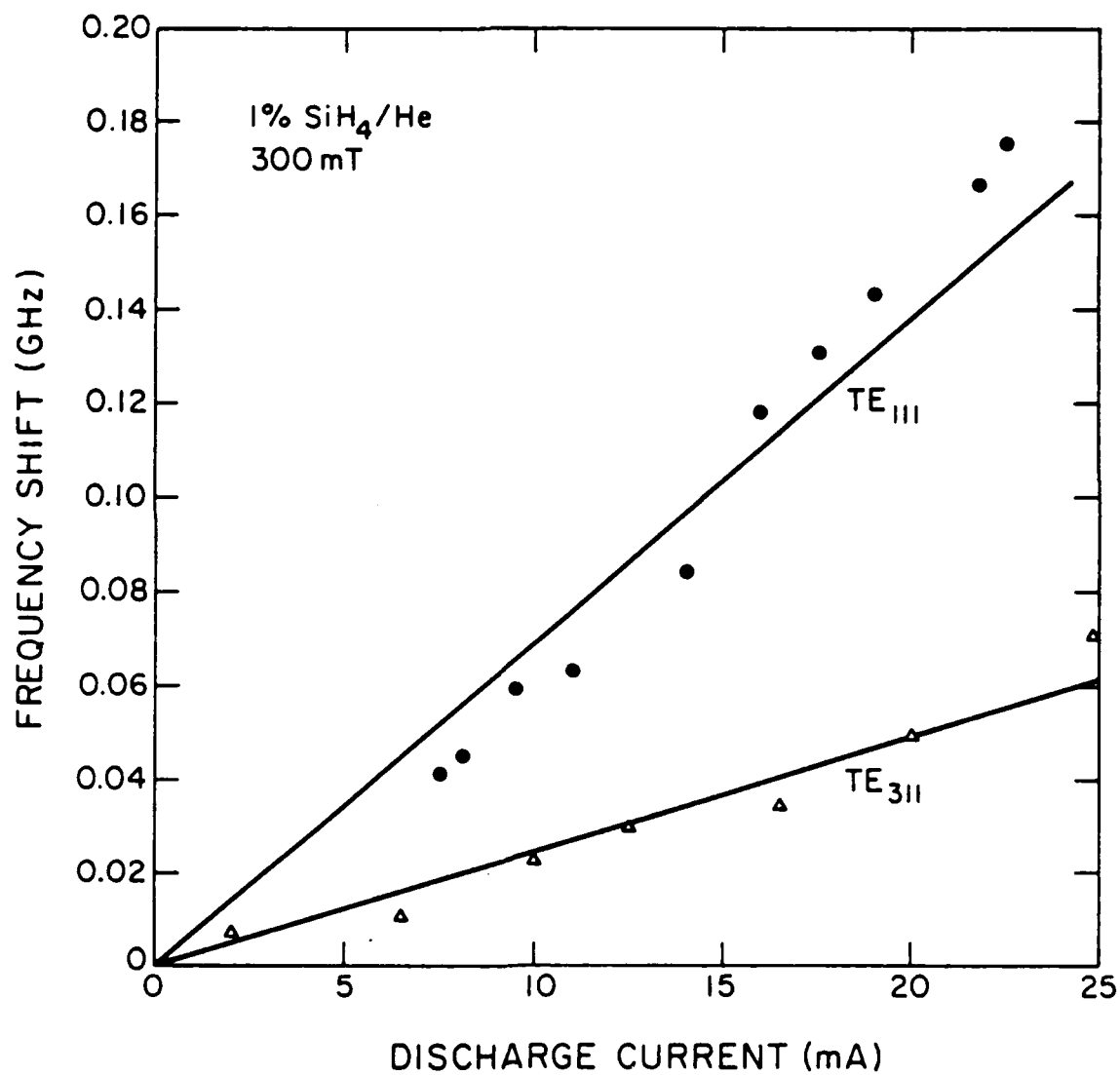


Fig. 13 Resonant frequency shift as a function of current for the TE_{111} and TE_{311} modes in 300 mT of 1% SiH₄ in helium.

(9). The results of this calculation for pure helium are shown in Fig. 14, where the axial electron density (the density of electrons at the center of the hollow cathode cylinder, or N_0) is plotted as a function of discharge current and helium pressure. The electron density increases linearly with discharge current, and is in the 10^{10} electrons/cm³ range, which is approximately as expected for a partially ionized medium at these pressures. Figure 14 also shows that the electron density increases approximately linearly with pressure in the system (for pressures in this range). This is also expected since increasing the pressure increases the density of neutrals available for ionization.

Figure 15 is a plot of the same type of data presented in Fig. 14, with the additional variable of percentage silane diluted in helium. The results are basically the same as before: there is a linear relationship between the electron density in the plasma and the discharge current. However, the effect of the addition of silane to the discharge is quite dramatic: the electron density is greatly reduced even for very small percentages of silane. Compared to 100% helium, there is approximately an order of magnitude decrease in electron density for just a 2% silane in helium mixture. This indicates that adding silane to the gas mixture greatly accelerates the loss rate for electrons in the discharge.

In order to understand the nature of this increased electron density decay, the functional dependence of the electron density with silane percentage must be considered. The increased density decay might be attributable to a difference in diffusion coefficient of the silane or silane product ions compared to helium ions, thus changing the rate of ambipolar diffusion of the electrons to the wall. The expression for

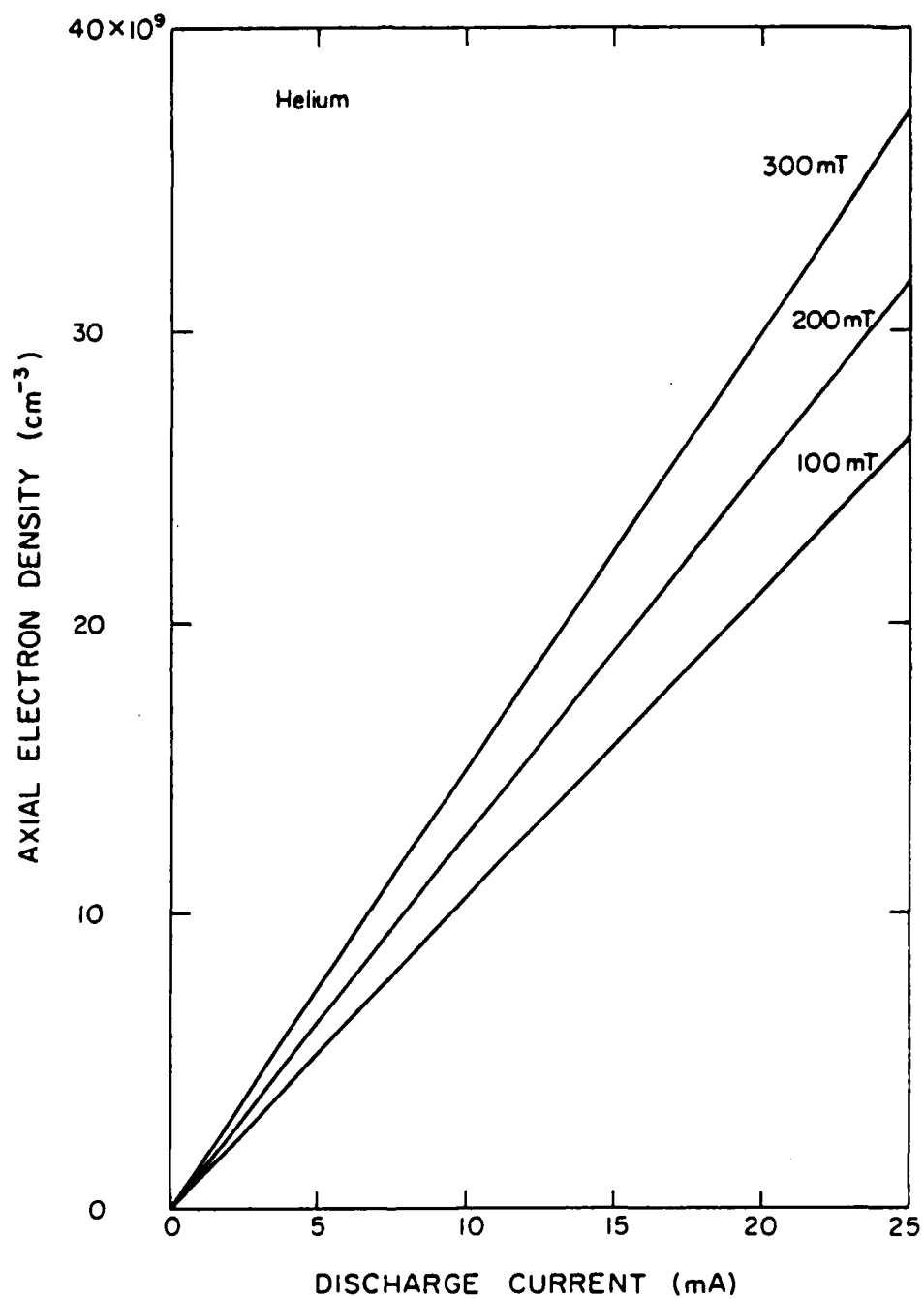


Fig. 14 Electron density vs. discharge current for pure helium discharge.

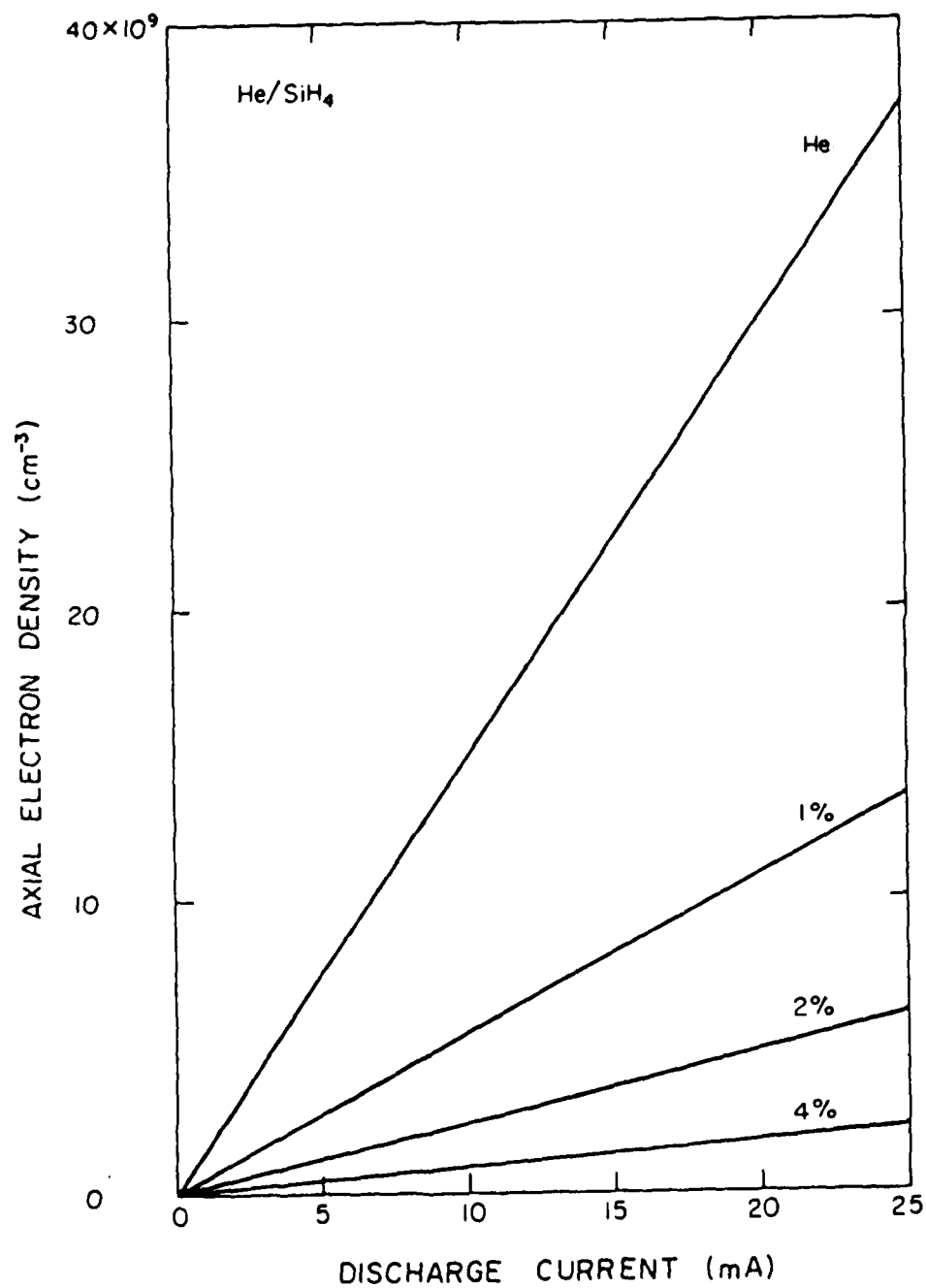


Fig. 15 Electron density vs. discharge current for helium and various concentrations of silane diluted in helium.

the ambipolar diffusion constant for electrons in a multi-species discharge is⁴¹

$$D_{a,e} = \frac{[He^+]}{N_e} D_{a,He^+} + \frac{[SiH_x^+]}{N_e} D_{a,SiH_x^+} \quad (10)$$

where $[He^+]$ and $[SiH_x^+]$ are the concentrations of helium ions and silane product ions, respectively. The rate equation for the electron loss, assuming a diffusional loss process, is

$$\frac{dN_e}{dt} = P - \frac{N_e}{\tau} \quad (11)$$

where P is the electron production term in $cm^{-3} sec^{-1}$ and τ is the diffusion time constant. For steady state (dc), the time derivative is zero and

$$N_e = P\tau \quad (12)$$

Substituting for τ gives

$$N_e = \frac{P}{A[\gamma D_{a,He^+} + (1-\gamma)D_{a,SiH_x^+}]} \quad (13)$$

where A is a geometrical constant and γ is the percentage helium in the gas mixture. From Equation (13), the variation in N_e with silane percentage for the low percentages shown in Fig. 15 would be quite

small, certainly smaller than the order of magnitude change shown in Fig. 15.

This suggests then, that the increased electron decay is instead attributable to a volumetric loss process such as recombination or attachment. At these pressures, recombination is an unlikely process, so we attribute this increased electron loss to dissociative attachment. Ignoring diffusion but including attachment, Equation (11) can be rewritten

$$\frac{dN_e}{dt} = P - k[X]N_e \quad (14)$$

where k is the rate coefficient for the attachment process and $[X]$ is the concentration of attaching species, which is directly related to the percentage silane in the gas mixture. Again, for steady state dN_e/dt is zero, so the solution for Equation (14) is

$$\frac{1}{N_e} = \frac{k[X]}{P} \quad (15)$$

which indicates a straight-line relationship between $1/N_e$ and percentage silane. Figure 16 is a plot of $1/N_e$ versus percent SiH_4 and, indeed, it is a straight line, which indicates that the predominant loss mechanism in the discharge is attachment, rather than diffusional losses to the wall.

Further evidence for the volumetric nature of the electron loss process is provided by consideration of the spatial electron density distribution, which is determined by the method outlined in Chapter 3.

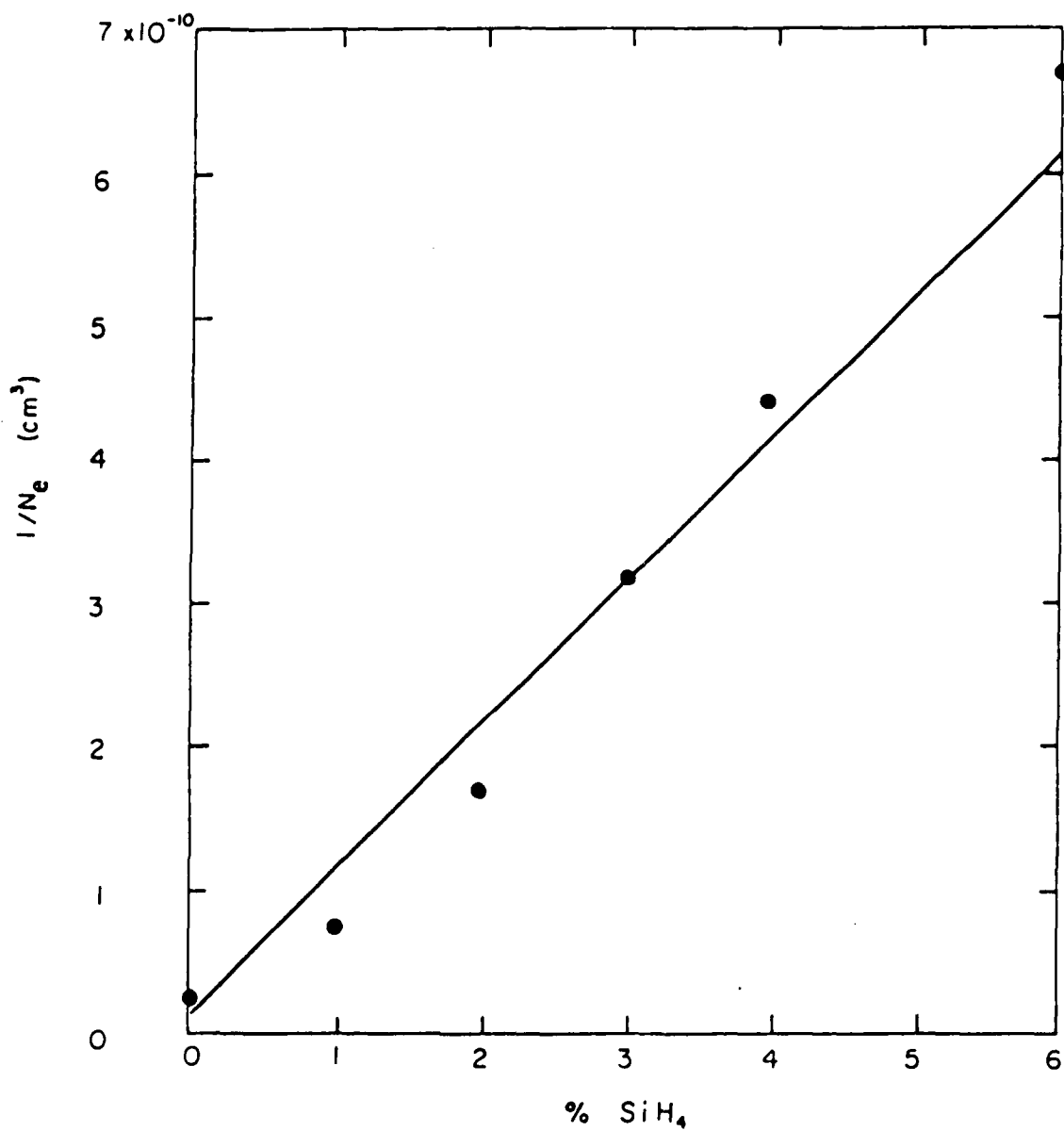


Fig. 16 Reciprocal of the electron density as a function of percentage silane.

Figure 17 shows the results of the computer analysis of the raw data and the determination of values for N_0 and m in Equation (9) for 100% helium at 300 mT for a hollow cathode current of 25 mA: electron density is plotted as a function of radial distance from the center of the hollow cathode, normalized to the radius of the hollow cathode. The profile shown in Fig. 17 indicates that the major electron loss process is due to diffusion to the walls, which is expected since helium is not an attaching gas and recombination is not a significant loss process in helium at 300 mT. In terms of the raw data, this radial profile is indicated by the much larger resonant frequency shift for the TE_{111} mode compared to that for the TE_{311} mode. This indicates a much larger density of electrons in the center of the cavity than out toward the walls. Consequently, the value for m is one, and the radial density distribution is rounded as expected for a diffusional loss process.

Figure 18 shows the same type of results as Fig. 17, except in this case silane is added to the discharge. In contrast to Fig. 17, in Fig. 18 there is a very noticeable flattening in the electron density profile as silane is added, in addition to the reduction in the overall magnitude of the electron density. In this case, the magnitude of the frequency shift for the TE_{311} mode becomes closer to that for the TE_{111} mode as silane is added to the discharge, indicating that the relative density of electrons near the walls is becoming comparable to the axial electron density. As the density of silane in the gas mixture increases, the value for m in Equation (9) increases, which is shown by the flattening of the curves. The type of profile shown in Fig. 18 is not characteristic of diffusion, but rather indicates that electrons are

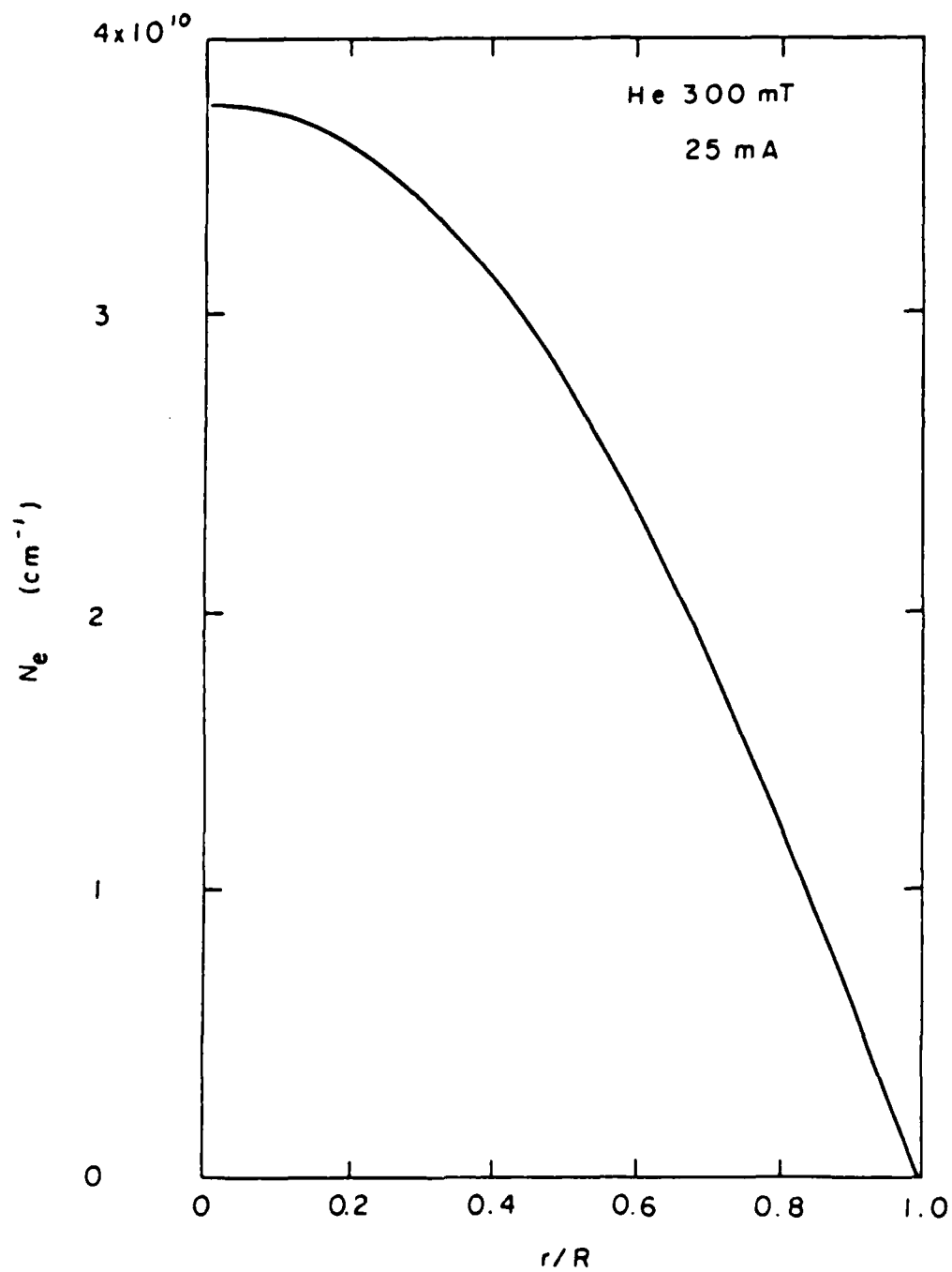


Fig. 17 Radial distribution of the electron density in helium.

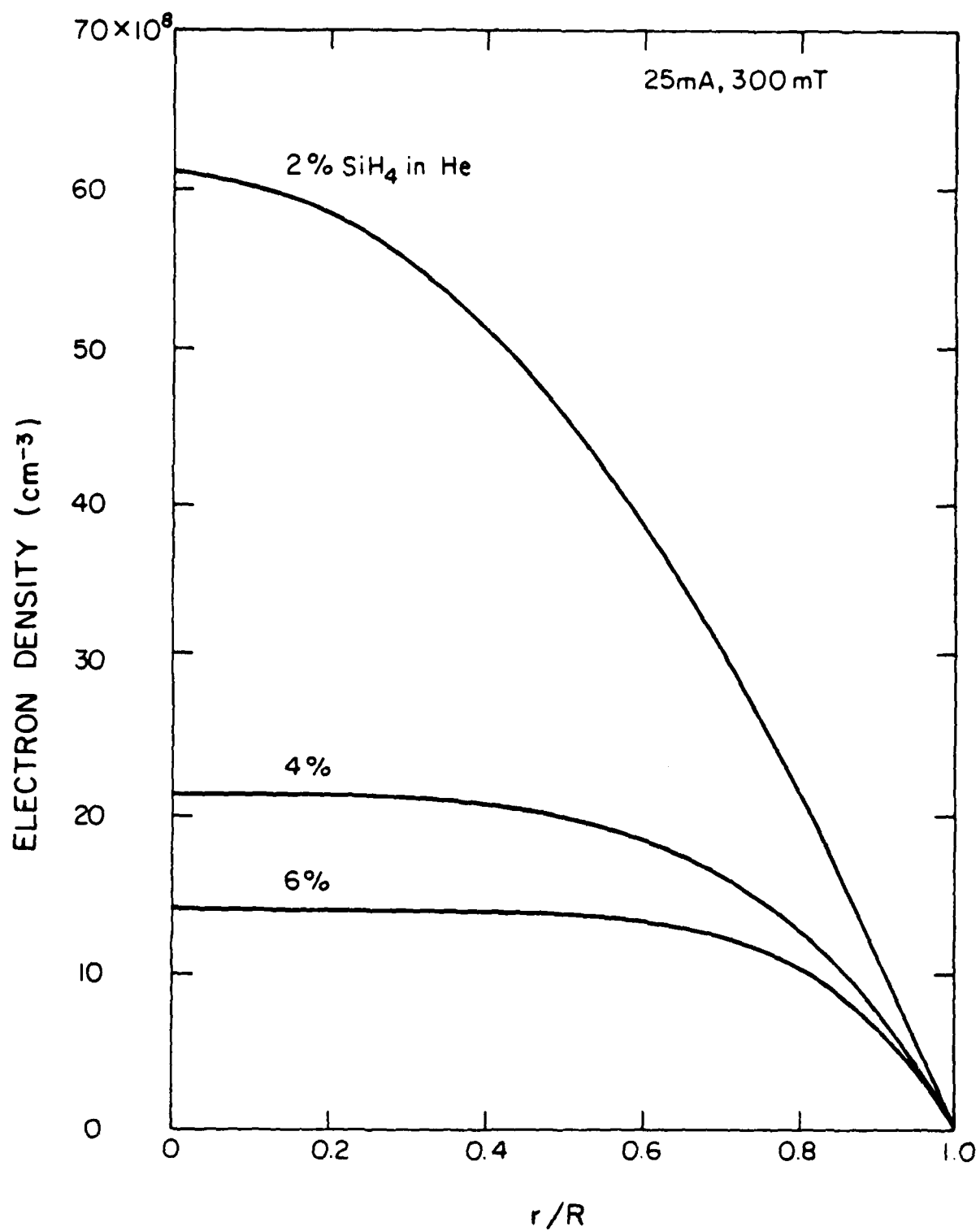


Fig. 18 Radial electron density distribution for various percentages of silane in helium.

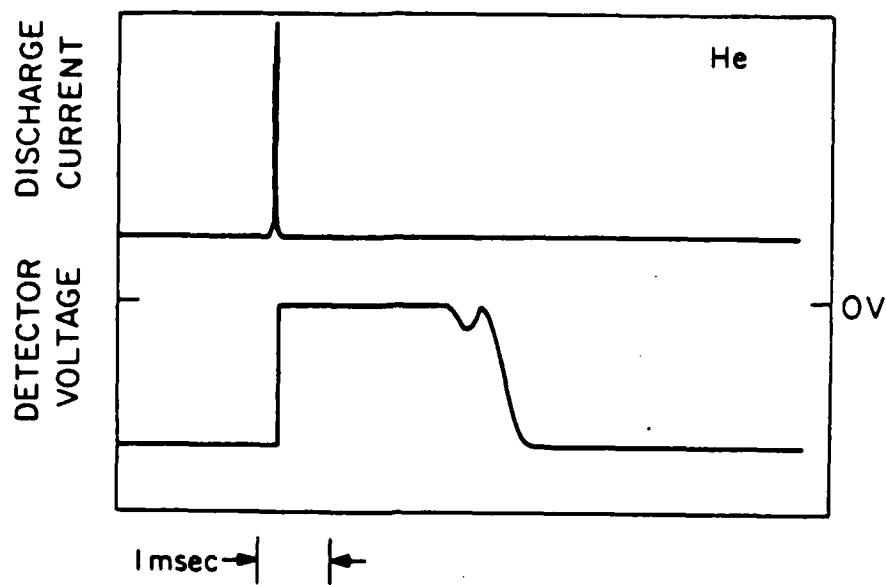
being lost before they have a chance to diffuse. In other words, there is a large volumetric loss of electrons in this discharge when silane is added to the gas mixture, which is indicated in Fig. 18 by the reduction in axial density compared to the density for $r \sim R$.

Having established that dissociative attachment is a very significant process in silane glow discharges, which causes a large reduction in the electron density, it is important to ascertain which of the species in the discharge is responsible for the attachment, and what the rate coefficient for the process is. In the next chapter, these issues will be addressed using the same microwave diagnostic technique with a pulsed hollow cathode discharge.

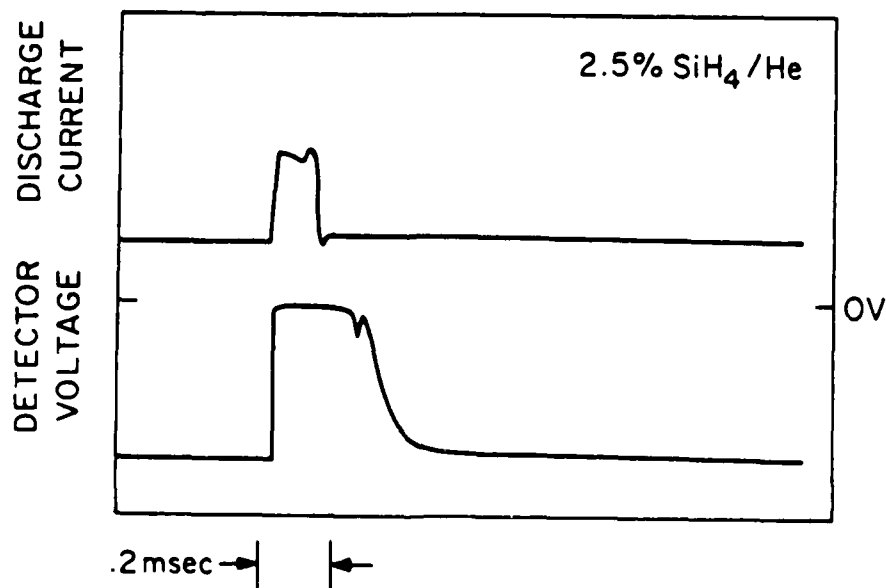
V. PULSED MEASUREMENTS

The attaching specie in the silane/helium discharge and the rate coefficient for the attaching process were determined by replacing the dc power supply used in Chapter 4 with a pulsed power supply. By pulsing the hollow cathode to create a plasma and measuring the resonant frequency of the cavity as a function of time in the afterglow, the time history of the electron density can be obtained.

Figure 19 shows typical oscilloscope tracings of the discharge current and the microwave detector voltage when the hollow cathode is pulsed. In Fig. 19, the microwave generator is set at the resonant frequency of the empty cavity, indicated by the negative voltage on the oscilloscope trace before the current pulse. When the hollow cathode is pulsed and a plasma is created, the resonant frequency of the cavity is shifted, so that the detector voltage goes to zero. Eventually, the electron density in the cavity decays and the cavity returns to resonance indicated by the return of the detector voltage to its initial negative value. If the frequency of the microwave generator is increased during the pulsed experiments, there is a dip in the oscilloscope trace which is due to the cavity becoming resonant at the electron density corresponding to the frequency of the microwave generator, giving a simultaneous measure of the electron density and the time at which that density occurs. By changing the frequency of the microwave generator and measuring the time of the corresponding dip in the detector voltage, the electron density as a function of time can be determined. From the time



(a)



(b)

Fig. 19 Oscillograms of the microwave detector voltage for pulsed discharge experiments.

history of the electron density in the afterglow, information about the nature of the attachment process can be obtained.

Figure 19a shows the results of these measurements for 100% helium. The time for the electron density to decay to zero is about 3 msec, in contrast to Fig. 19b where a 2.5% silane/helium gas mixture has been used, and the decay time is greatly reduced to around 0.2 msec. This supports the results obtained in the previous chapter that the presence of silane greatly increases the electron loss rate in the plasma. This is shown more clearly in Fig. 20, a plot of the time dependence of the electron density for pure helium and for a 5% SiH_4/He mixture, both at 300 mT. The time constant for the decay in pure helium is on the order of hundreds of microseconds, characteristic of electron loss by ambipolar diffusion to the walls. When silane is added to the gas mixture, even in small amounts, there is a very noticeable increase in the rate of electron density decay. In Fig. 20, the decrease in decay time constant is over an order of magnitude for a 5% silane in helium mixture.

For a given SiH_4 concentration in the input gas mixture, the decay time was found to be a function of the pulse width and the pulse current. The time history of the electron density for different excitation pulse widths is illustrated in Fig. 21, which shows that the decay time constant is very dependent on pulse width. This dependence is plotted in Fig. 22 for 300 mT of a 5% SiH_4/He mixture, showing that an increase in the pulse width applied to the discharge causes a decrease in the decay time constant. Similar behavior is observed when the current in the pulse is increased while holding the pulse width and

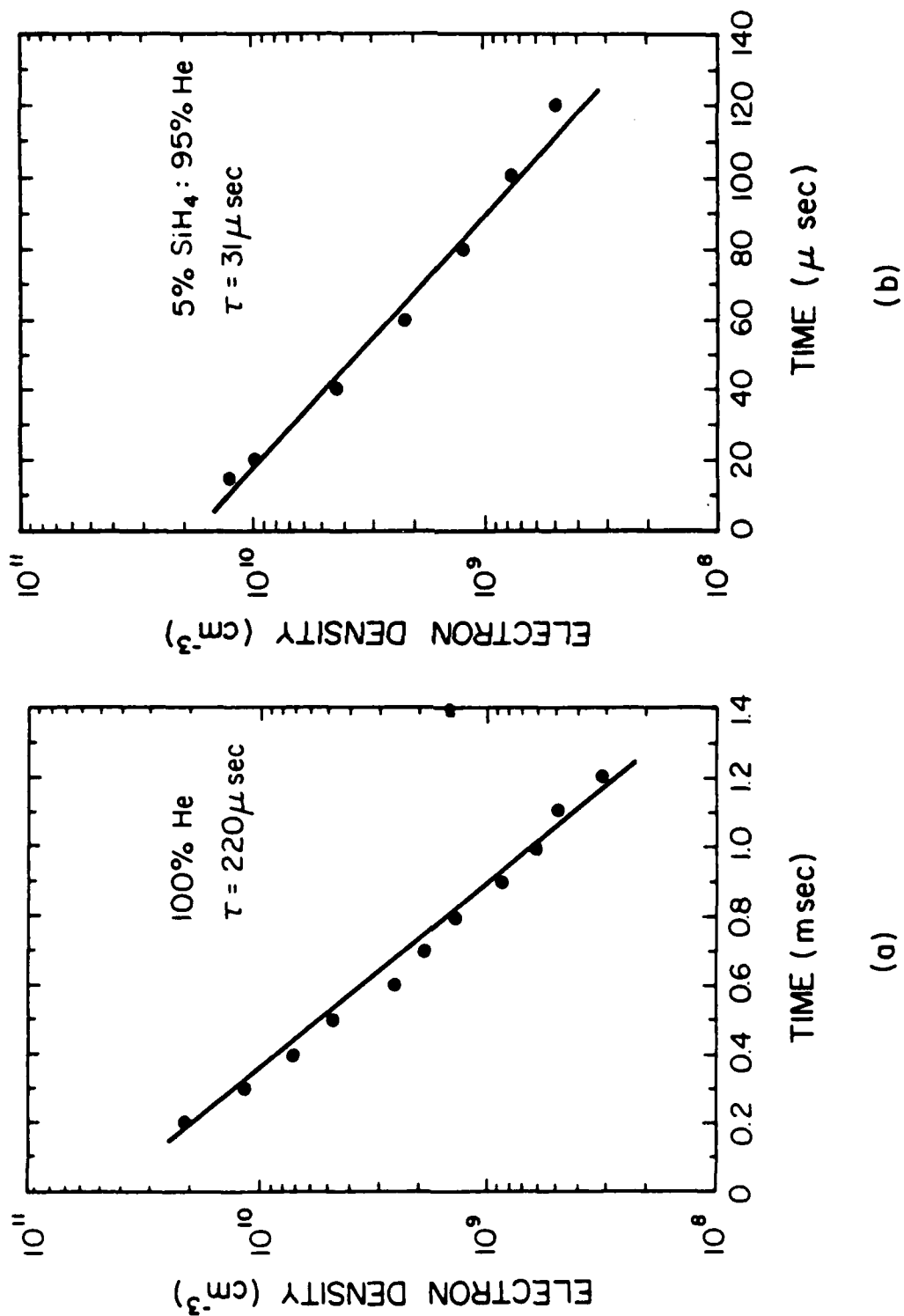


Fig. 20 Time dependence of the electron density in the afterglow of He and 5% SiH₄ in He discharges.

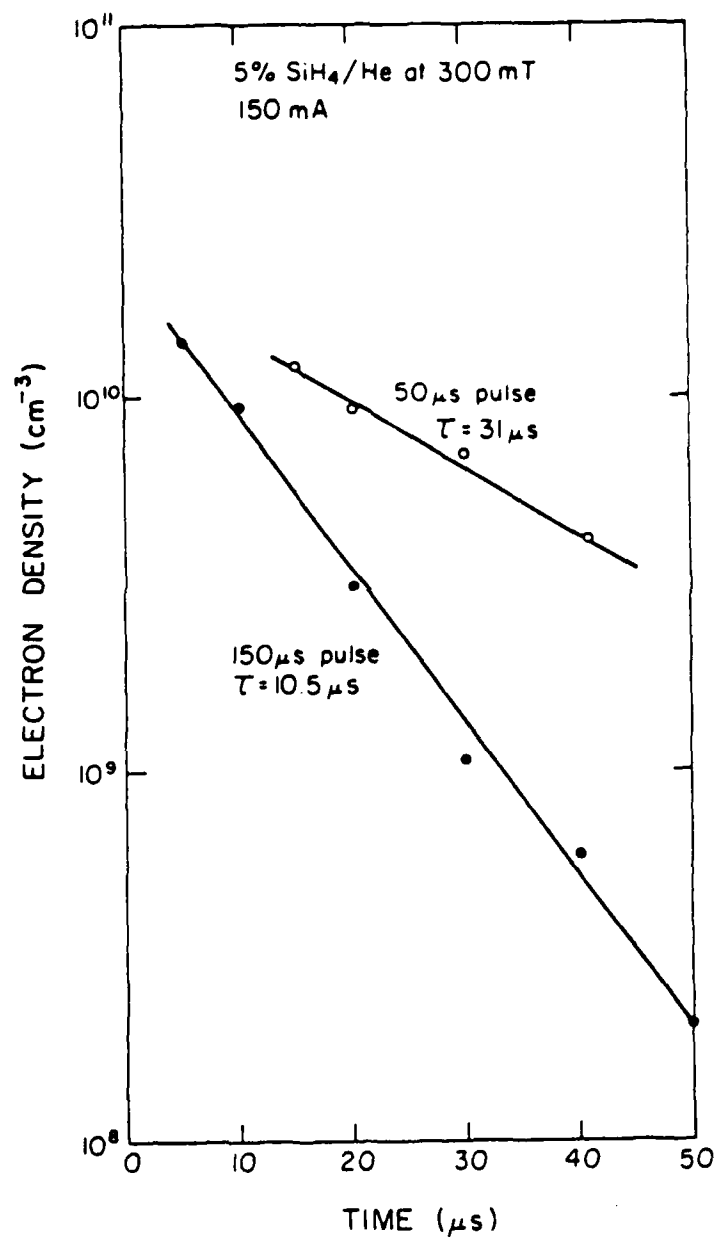


Fig. 21 Time dependence of electron density for two different excitation pulse widths.

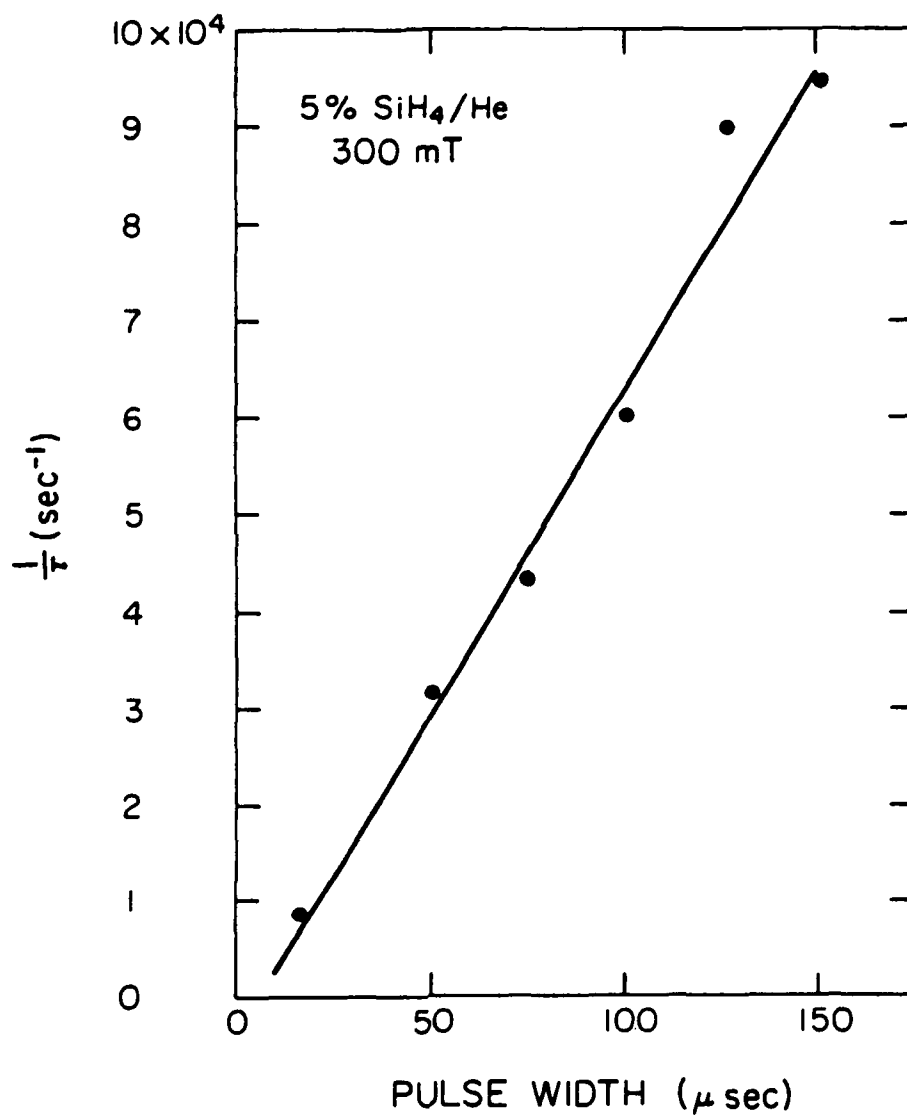


Fig. 22 Functional dependence of electron density decay time constant on excitation pulse width.

voltage constant: the decay time decreases with increasing current. The effect of increasing pulse width and pulse current is to increase the dissociation of the parent SiH_4 molecules, thus reducing the SiH_4 molecule density in the plasma. Since the decay constant increases as the dissociation of SiH_4 increases, it is concluded that the electron attachment is due primarily to some product specie of the dissociation of SiH_4 (SiH_x or H_2), and that attachment to SiH_4 is not significant in these experiments.

A quadrupole mass spectrometer was used to determine the relative concentration of the various dissociation products of silane. Distinct peaks were observed for H , H_2 , SiH , SiH_2 , and SiH_3 . The height of the peak corresponding to molecular hydrogen indicated that H_2 is a major dissociation product of silane in this discharge, so experiments were performed to determine whether dissociative attachment to H_2 is a factor in the large electron loss in silane discharges. The silane/helium mixture used previously was replaced by molecular hydrogen diluted in helium. The result of measurements of the reciprocal time constant vs. percent H_2 is shown in Fig. 23, and shows that as H_2 is added to helium, the time constant for electron decay increases, which is readily accounted for by the lower diffusion constant of H_2^+ in helium compared to He^+ .⁴² Similar experiments were performed by adding H_2 to the 5% SiH_4/He mixture, with the result that again the time constant for electron loss increased. This indicates very clearly that dissociative attachment to H_2 produced from the dissociation of SiH_4 is not a significant process in silane discharges. The mass spectroscopic measurements also showed that the peak corresponding to SiH was very

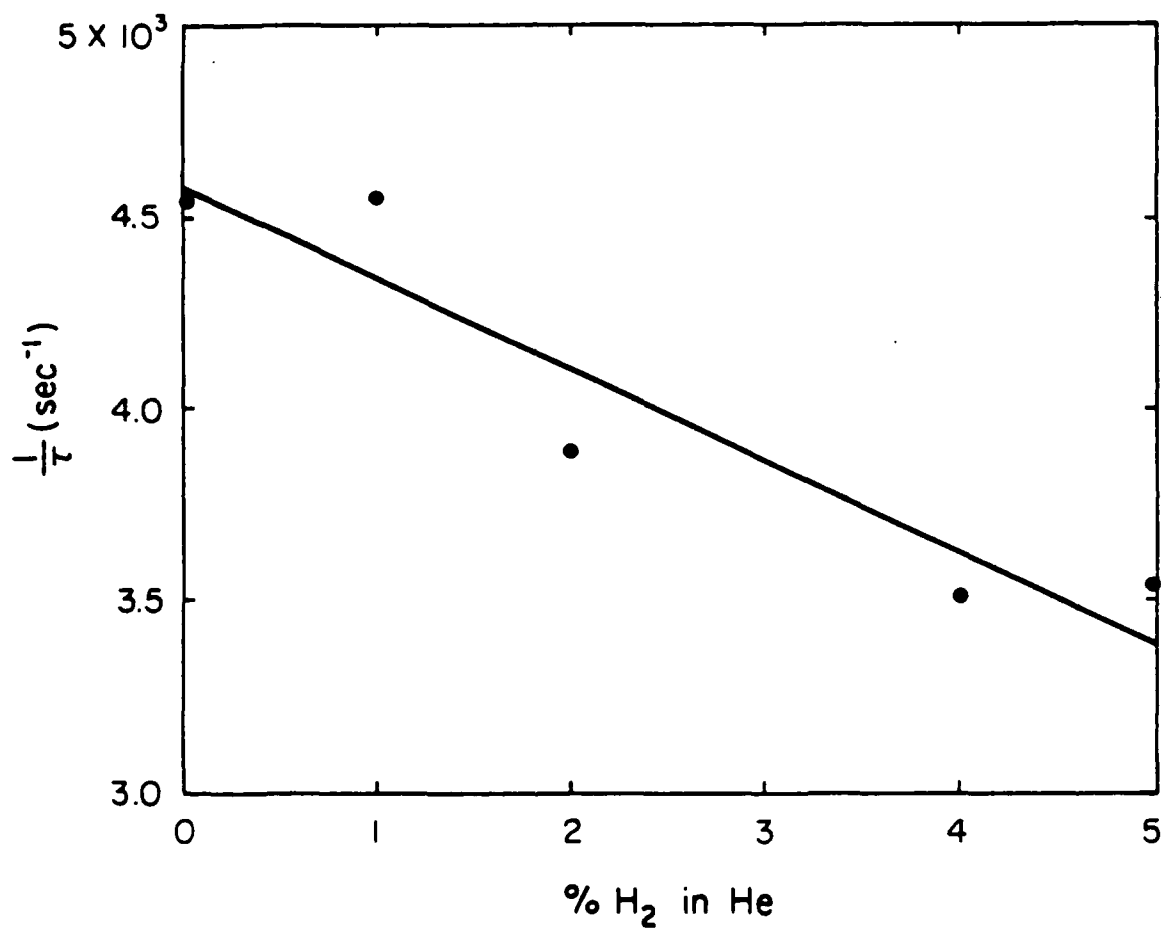


Fig. 23 Dependence of decay time on percentage hydrogen diluted in helium.

small, but those for SiH_2 and SiH_3 were roughly equal in height, and over an order of magnitude higher than that for SiH . From this we conclude that the primary dissociative attachment process is to SiH_2 , SiH_3 , or possibly both.

The functional dependence of the time constant on pulse width can be calculated by considering the rate equations for dissociation and attachment in the plasma. It is assumed that the major dissociation process is electron impact dissociation of silane (Equation (2), where SiH_x is the attaching specie SiH_2 or SiH_3). The pertinent rate equations are

$$\frac{d[\text{SiH}_4]}{dt} = -CI [\text{SiH}_4] \quad (16a)$$

$$\frac{d[\text{SiH}_x]}{dt} = CI [\text{SiH}_4] \quad (16b)$$

$$\frac{dN_e}{dt} = -k [\text{SiH}_x] N_e \quad (16c)$$

where I is the discharge current, C is a constant, and k is the attachment rate coefficient. Equations (16a) and (16b) describe the dissociation process, and (16c) describes the attachment of electrons by the dissociation product. In using Equation (16), it is assumed that these processes are fast compared to the flow of gases in the system. Experimentally, this means that the pulse repetition rate has been

slowed sufficiently to ensure that there is a fresh fill of gas every time the hollow cathode is pulsed. The solution to Equation (16a) is

$$[\text{SiH}_4] = [\text{SiH}_4]_0 e^{-CI t} \quad (17)$$

Substituting (17) into Equation (16b) gives

$$\frac{d[\text{SiH}_x]}{dt} = CI [\text{SiH}_4]_0 e^{-CI t} \quad (18)$$

so that

$$[\text{SiH}_x] = CI [\text{SiH}_4]_0 \int_0^{t_p} e^{-CI t} dt \quad (19)$$

where t_p is the duration of the current pulse, leading to a value for the attaching species density of

$$[\text{SiH}_x] = CI [\text{SiH}_4]_0 (1 - e^{-CI t_p}) \quad (20)$$

The solution to Equation (16c) is

$$N_e = N_{e,0} e^{-k[\text{SiH}_x]t} \quad (21)$$

Thus, the time constant for the electron density decay due to attachment may be written

$$\frac{1}{\tau} = k[\text{SiH}_x] = k [\text{SiH}_4]_0 (1 - e^{-CI\tau p}) \quad (22)$$

which expresses the time constant in terms of the external discharge parameters. A comparison of this theoretical expression with experimental results is shown in Fig. 24. The data points were obtained using the method outlined previously, and the solid lines were obtained by using a least squares fit to the 0.5% silane data in order to obtain a value for CI, and then generating the curves for the other three silane percentages using Equation (22). The agreement between the theoretical and experimental values in Fig. 24 is excellent, further confirming that dissociative attachment to a product specie of the silane dissociation is the predominant electron loss process in silane discharges. The 0.25% experimental results are slightly higher than the theory predicts, which is attributed to the fact that at such a low percentage silane, the losses due to diffusion start to become comparable to those for attachment, thus lowering the time constant below the expected value.

Using the data from Fig. 24, it is possible to estimate the rate coefficient (k) for the dissociative attachment process in this plasma. The density of the SiH_4 parent molecule is known from the pressure and the percent silane in the gas mixture. Using Equation (22) for large values of t_p , k is determined by dividing the reciprocal time constant by the silane density. Using the large pulse width values of $1/\tau$ from Fig. 24, we estimate a rate coefficient for this process of

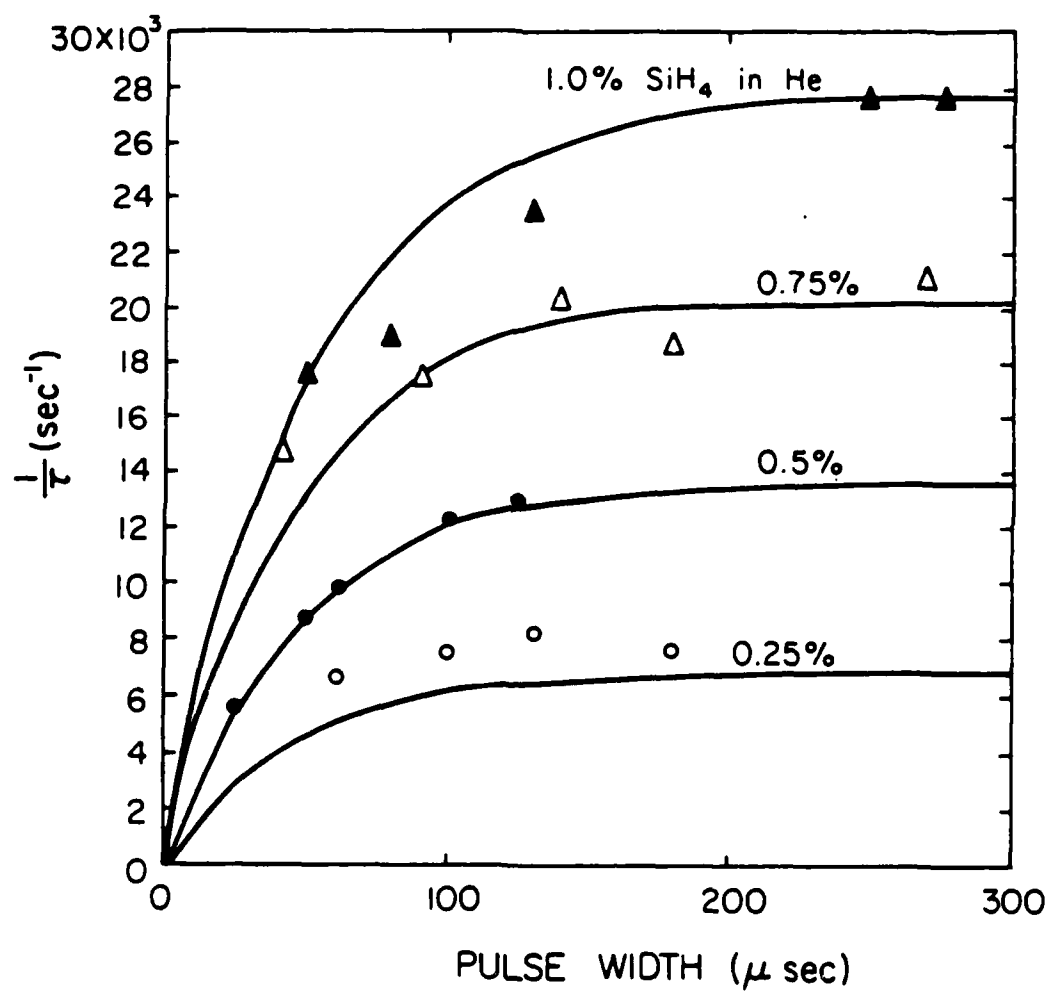
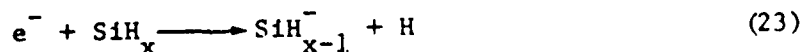


Fig. 24 Variation of electron density decay time on pulse width and percentage silane for very low silane densities.

$2.65 \pm 0.19 \times 10^{-10} \text{ cm}^3/\text{sec}$. The assumption that all the input silane is dissociated into an attaching specie, which is implicit in Equations (16a) and (16b), is only an approximation, so the density of attaching species is likely to be somewhat smaller than the input silane density. Thus, the estimate obtained is a lower bound on the real value of k . However, since the mass spectrometric measurements show an equal amount of SiH_2 and SiH_3 and very little SiH , this value for k is probably off by no more than a factor of 2.

VI. SUMMARY AND CONCLUSIONS

The work described in the previous chapters was undertaken to measure the electron density in silane/helium plasmas, and from these measurements to identify important kinetic processes and reaction pathways in the silane discharge. The major results of these measurements can be summarized as follows: the electron density in silane/helium discharges decreases dramatically when silane is added to helium; the larger the silane percentage, the larger the decrease in the electron density. Since silane and many of its dissociation products are electronegative, this phenomenon can be readily accounted for by a process of dissociative attachment of electrons. Studies using a pulsed discharge show that silane itself is not the dominant specie responsible for the attachment, but rather the attachment is through some product of the dissociation of silane. Molecular hydrogen is also ruled out by similar pulsed studies, and SiH is an unlikely candidate due to its relatively low density in the discharge. This suggests that the dissociative attachment process is to SiH₂, SiH₃, or both, and is described by



where x is either 2 or 3. The rate coefficient for this process was measured to be $2.65 \times 10^{-10} \text{ cm}^3/\text{sec}$.

These results have very important implications for the

understanding and modeling of silane discharges and the deposition process. A decrease in electron density fundamentally changes the plasma environment by lowering the plasma potential, changing the electron energy distribution, and thus altering reaction pathways. The rate coefficient determined in this study for the dissociative attachment process is a significant fraction of the value derived from the literature for the rate coefficient for electron impact dissociation of silane ($\sim 10^{-9}$ cm³/sec).⁴³ Thus, the attachment process described by Equation (23) is in direct competition with the dissociation of silane, which provides the raw material for amorphous silicon film growth. Clearly, the loss of electrons due to this process has a significant effect on the properties of the discharge plasma and the films grown in discharge systems, and should be included in comprehensive models of the silane glow discharge. Moreover, the fact that relatively large densities of negative ions are being formed in the plasma might have some bearing on the differences between films grown on the cathode and the anode, and also on the possibilities of reactions between negative ions and neutrals in the discharge, both of which have only been speculated upon in the literature.

The work reported here has shown that dissociative attachment is a very important process in silane discharges, one that has been virtually ignored in models of silane plasmas. The inclusion of this process should lead to more realistic (and one hopes, more useful) models of the deposition of amorphous silicon from glow discharges.

REFERENCES

1. D. L. Flamm, V. M. Donnelly, D. E. Ibbotson, J. Vac. Sci. and Technol. B 1, 23 (1983).
2. M. J. Helix, K. V. Vaidyanathan, B. G. Streetman, H. B. Dietrich, P. K. Chatterjee, Thin Solid Films 55, 143 (1978).
3. C. Weissmantel, Thin Solid Films 58, 101 (1979).
4. K. I. Dirov, S. S. Georgiev, B. G. Pantchev, J. B. Kobrinarova, Thin Solid Films 72, L9 (1980).
5. R. Chittick, J. Alexander, H. Sterling, J. Electrochem. Soc. 116, 77 (1969).
6. W. Spear, P. LeComber, Solid State Comm. 17, 1193 (1975).
7. P. J. Zanzucchi, C. R. Wronski, D. E. Carlson, J. Appl. Phys. 48, 5227 (1977).
8. M. Wolf, Solar Cells 12, 231 (1984).
9. A. Catalano, R. V. D'Aiello, J. Dresner, B. Faughnan, A. Firester, J. Kane, H. Schade, Z. E. Smith, G. Swartz, A. Triano, Sixteenth IEEE Photovoltaic Specialists Conference, IEEE, New York (1982), p. 1421.
10. M. B. Spitzer, C. J. Keavney, S. P. Tobin, J. B. Milstein, Seventeenth IEEE Photovoltaic Specialists Conference, IEEE, New York (1984), p. 398.
11. P. G. LeComber, A. J. Snell, K. D. MacKenzie, W. E. Spear, J. Physique 42, C4, 423 (1981).
12. K. D. MacKenzie, A. J. Snell, I. French, P. G. LeComber, W. E. Spear, Appl. Phys. A 31, 8 (1983).

13. I. French, A. J. Snell, P. G. LeComber, J. Stephens, Appl. Phys. A 31, 19 (1983).
14. B. Abeles, T. Tiedje, Phys. Rev. Lett. 51, 2003 (1983).
15. J. C. Knights, R. A. Lujan, M. D. Rosenblum, R. A. Street, D. K. Biegleson, J. A. Reimer, Appl. Phys. Lett. 38, 331 (1981).
16. J. E. Potts, E. M. Peterson, J. A. McMillan, J. Appl. Phys. 52, 6665 (1981).
17. B. Drevillon, J. Huc, A. Lloret, J. Perrin, G. de Rosny, J. P. M. Schmitt, Appl. Phys. Lett. 37, 646 (1980).
18. R. Robertson, D. Hils, H. Chatham, A. Gallagher, Appl. Phys. Lett. 43, 544 (1983).
19. G. Turban, Y. Catharine, B. Grolleau, Thin Solid Films 60, 147 (1979).
20. G. Turban, Y. Catharine, B. Grolleau, Thin Solid Films 67, 309 (1980).
21. I. Haller, Appl. Phys. Lett. 37, 282 (1980).
22. H. A. Weakliem, R. D. Estes, P. A. Longeway, in Proc. of the Sixth Int. Symp. on Plasma Chem., (Montreal, 1983) ed. by M. I. Boulos and R. J. Munoz, (McGill Univ., Montreal, 1983) p. 388.
23. K. P. Wanczek, Int. J. Mass Spect. Ion Proc. 60, 11 (1984).
24. P. Haaland, A. Rahbee, presented at the 37th Annual Gaseous Electronics Conference, Boulder (1984).
25. F. J. Kampas, J. Appl. Phys. 54, 2276 (1983).

26. M. Hirose, T. Hamasaki, Y. Mishima, H. Kurata, Y. Osaka, Proc. of Conf. on Tetrahedrally Bonded Amorphous Semiconductors, (Cafree, Arizona, 1981) ed. by R. A. Street, D. K. Biegleson, J. C. Knights, (American Institute of Physics, New York, 1981) p. 10.
27. A. Mitsuda, K. Nakagawa, K. Tanaka, M. Matsumura, S. Yamasaki, H. Okushi, S. Iizima, J. Non-Cryst. Solids 35-36, 183 (1980).
28. P. Kocian, J. M. Mayor, S. Bourquard, Fourth Int. Symp. on Plasma Chem., Zurich (1979) p. 663.
29. P. Kocian, J. Non-Cryst. Solids, 35-36, 195 (1980).
30. G. Gleres, in Proc. of the Sixth Int. Symp. on Plasma Chem., (Montreal, 1983) ed. by M. I. Boulos and R. J. Munoz, (McGill Univ., Montreal, 1983) p. 456.
31. A. Garscadden, in Proc. of the Sixth Int. Symp. on Plasma Chem., (Montreal, 1983) ed. by M. I. Boulos and R. J. Munoz, (McGill Univ., Montreal, 1983) p. 388.
32. For example: D. E. Carlson in The Physics of Amorphous Silicon I, ed. by J. D. Joannopoulos and G. Lucovsky (Springer-Verlag, Berlin, 1984) p. 203.
33. J. E. Smith, Jr., M. H. Brodsky, B. L. Crowder, M. I. Nathan, A. Pinczuk, Phys. Rev. Lett. 26, 642 (1971).
34. J. H. Parker, Jr., D. W. Feldman, M. Ashkin, Phys. Rev. 155, 712 (1967).
35. M. H. Brodsky, M. Cordona, J. J. Cuomo, Phys. Rev. B 16, 3556 (1977).
36. J. C. Knights, G. Lucovsky, R. J. Nemanich, Phil. Mag. B 37, 467 (1978).
37. J. Tauc, in Optical Properties of Solids, ed. by F. Abeles (North-Holland, Amsterdam 1970).

38. C. D. Cody, C. R. Wronski, B. Abeles, R. B. Stephens, B. Brooks, Solar Cells 2, (1980).
39. A. Gilardini, Low Energy Collisions in Gases, Wiley, New York (1972).
40. E. C. Jordan, K. G. Balmain, Electromagnetic Waves and Radiating Systems, Prentice-Hall, Englewood Cliffs, N.J. (1968).
41. B. E. Cherrington, Gaseous Electronics and Gas Lasers, Pergamon Press, Oxford (1979).
42. H. S. W. Massey, Electronic and Impact Phenomena, Oxford, London (1971).
43. A. Garscadden, G. L. Duke, W. F. Bailey, Appl. Phys. Lett. 43, 1012 (1983).

SECTION III

MEASUREMENT OF THE ELECTRON DENSITY AND THE ATTACHMENT
RATE COEFFICIENT IN SILANE/HELIUM DISCHARGES

by

C. B. Fledderman
J. H. Beberman
J. T. Verdeyen

April 1985

Measurement of the electron density and the attachment rate coefficient in silane/helium discharges

C. B. Fleddermann, J. H. Beberman, and J. T. Verdeyen

Department of Electrical and Computer Engineering, University of Illinois at Urbana-Champaign, Urbana, Illinois 61801

(Received 11 February 1985; accepted for publication 17 April 1985)

Measurements of the electron density in dc and pulsed silane/helium discharges show that the addition of silane to the gas mixture causes a large reduction in the electron density. By monitoring the electron decay time in the afterglow, it is found that the dominant electron loss mechanism in silane/helium is not ambipolar diffusion to the walls, but instead is a volumetric loss process, most likely dissociative attachment of electrons to a product of the silane dissociation. A lower bound for the rate coefficient for this loss process has been determined to be $2.65 \times 10^{-10} \text{ cm}^3/\text{sec}$.

I. INTRODUCTION

The use of glow discharges for the deposition of amorphous silicon has spurred many studies of deposition plasmas, including studies of the positive ionic species.¹⁻⁵ However, negative ions in silane plasmas have been largely ignored. This is a significant omission since the formation of negative ions can greatly affect the plasma kinetics by reducing the electron density, lowering the plasma potential, and by altering reaction pathways. In silane deposition plasmas, there are several possible negative ion formation paths, and these processes should be accounted for in any complete model of the deposition of amorphous silicon. In this paper, we describe experiments using microwave diagnostic techniques to measure the electron density and the decay rate of the electron density in silane/helium discharges to determine what negative ion formation processes are taking place, and to determine the rate coefficients for these processes.

II. EXPERIMENTAL APPARATUS

The experimental apparatus used in this study is shown schematically in Fig. 1. The electron density was measured in a discharge in a hollow cathode that also serves as a microwave cavity. The hollow cathode configuration was chosen both to facilitate the microwave measurements and because the hollow cathode discharge is sustained in a manner somewhat similar to the rf discharge.⁶ Thus, the results obtained here should be equally applicable to rf deposition systems. The hollow cathode/cavity is a 9.8 cm inner diameter stainless steel cylinder, 17.5 cm long, with two stainless steel end plates, each with a 2.5 cm centered hole to allow gas flow. Loop antennae are used to excite the cavity, to detect the microwaves in the cavity, and also serve as grounded anodes.

Two cavity modes were used in making these measurements: the TE_{111} mode with a resonance at 1.955 GHz and the TE_{311} mode at 4.071 GHz. The cavity Q was measured to be 980 and 580 for the 111 and 311 modes, respectively. The TE_{111} and TE_{311} modes have very different field configurations, shown in Fig. 2. The TE_{111} mode emphasizes the central core of the electron density distribution, whereas the TE_{311} mode emphasizes the electron density closer to the wall. Hence, measurements using both modes are comple-

mentary and allow an inference of the spatial distribution of the electron density. For the measurements reported here, the current densities ranged from 40 to 200 $\mu\text{A}/\text{cm}^2$, with dc and pulsed voltages of between 500 and 1000 V (depending on the composition and the pressure of the gas) applied to the hollow cathode.

The electron density is determined by measuring the shift in resonant frequency of the cavity due to the interaction of the microwave electric field with the free electrons in the plasma. Using a simple perturbation theory⁷ the electron density is found to be directly proportional to the shift in resonant frequency and is given by

$$\bar{N}_e = \frac{2m\epsilon_0(2\pi f_0)^2}{e^2} \frac{\Delta f}{f_0}, \quad (1)$$

where \bar{N}_e is the spatially averaged electron density, f_0 is the resonant frequency of the cavity, and Δf is the resonant frequency shift. Due to the nonuniformity of the electron density N_e , the average electron density is obtained by weighting N_e by the electric field

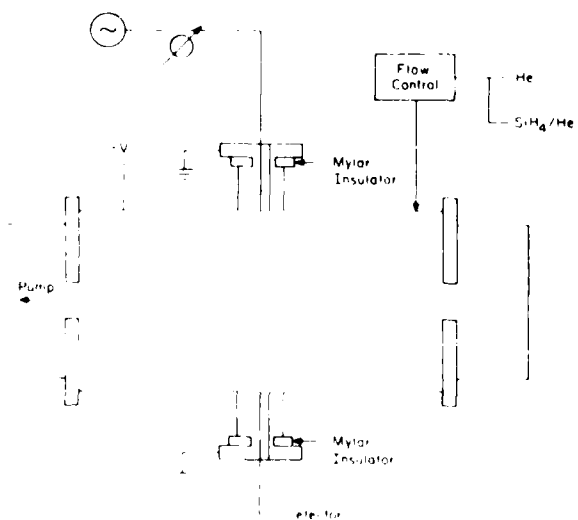


FIG. 1. Experimental setup for measuring electron density in a hollow cathode discharge.

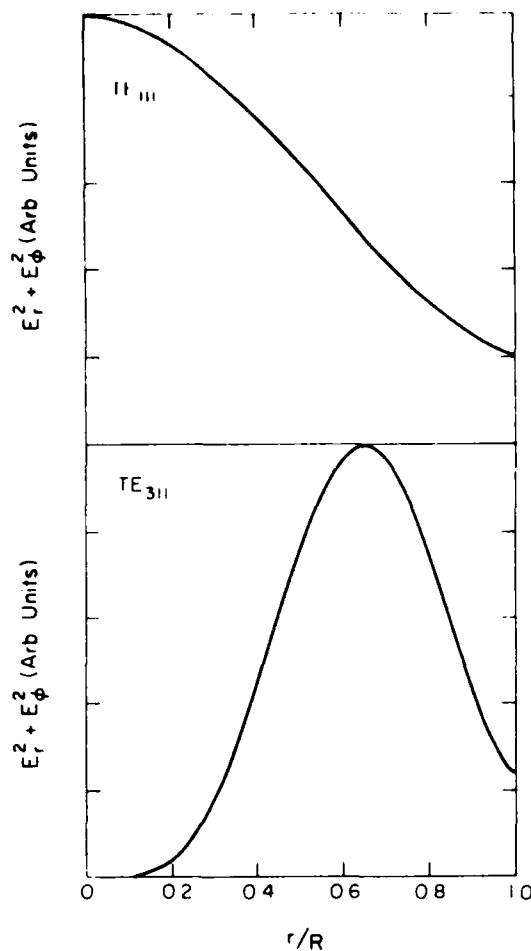


FIG. 2. Sum of the radial and circumferential electric field components for the TE_{111} and TE_{311} modes.

$$\bar{N}_e = \frac{\int_0^R N_e E_0^2 dV}{\int_0^R E_0^2 dV} \quad (2)$$

We assume a radial distribution given by

$$N_e = N_0 [1 - (r/R)^{2m}], \quad (3)$$

where N_0 is the electron density at the central axis of the cavity and R is the radius of the cavity. (For this distribution the electron density is highest at the center and decreases to zero as r approaches R .) It is also assumed that the variation of the electron density in the z direction can be ignored since the cavity is long compared to the sheath thicknesses at the end plates. Using Eqs. (1)–(3) and the resonant frequency shift measurements for the two modes, a computer was used to determine the values for N_0 and m , and hence the spatial distribution for all discharge conditions.

III. dc MEASUREMENTS

The resonant frequency shift as a function of discharge current for a typical discharge is shown in Fig. 3. This is the

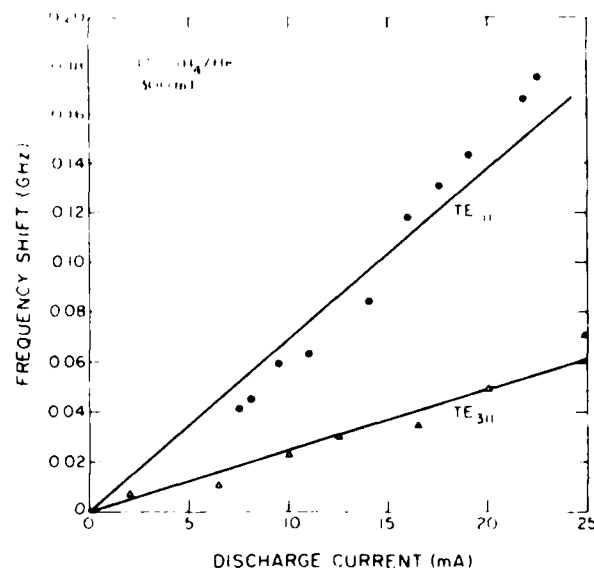


FIG. 3. Resonant frequency shift of the microwave cavity as a function of discharge current for TE_{111} and TE_{311} modes.

raw data that is fed into the computer to determine N_0 and m . The result of that computation is shown in Fig. 4 for pure helium and various silane percentages. As expected, the electron density increases with increasing current. However, the electron density decreases very rapidly as silane is added to the discharge, being reduced by nearly an order of magni-

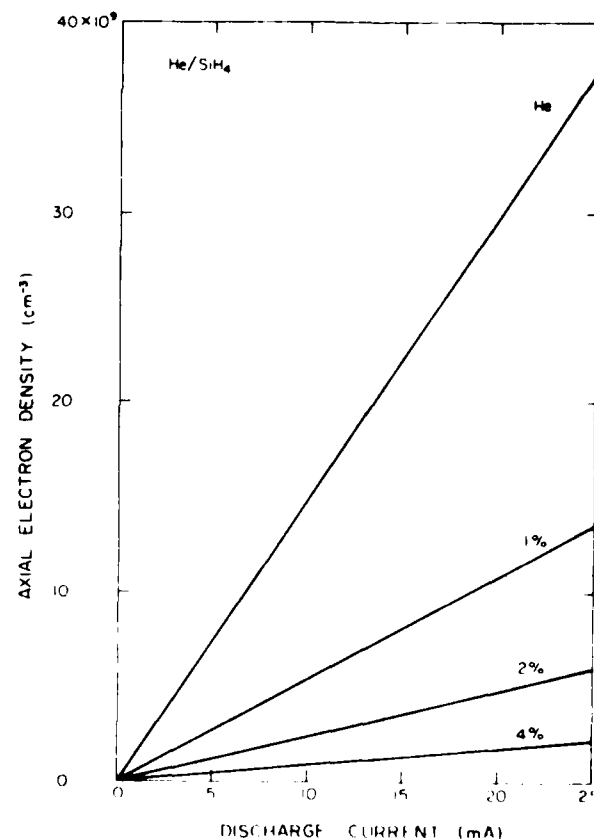


FIG. 4. Electron density vs current for helium and silane/helium mixtures.

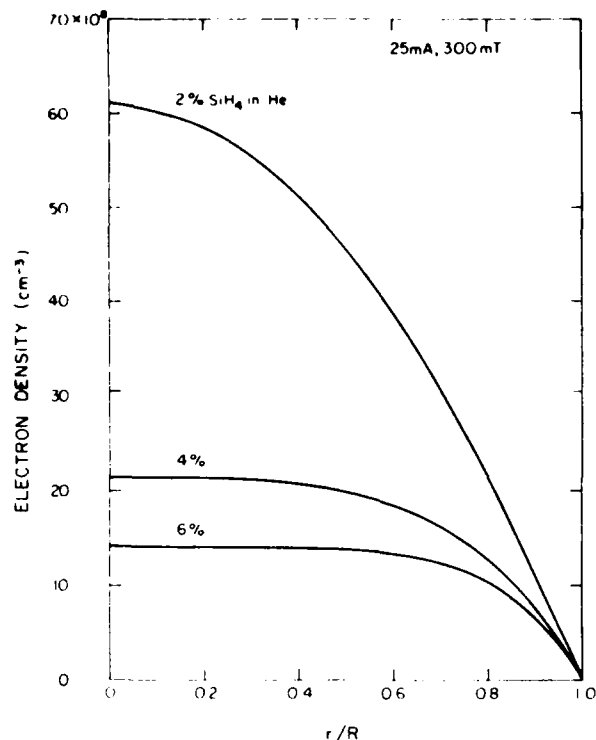


FIG. 5. Radial electron density distribution for silane/helium mixtures.

tude for as little as 2% silane. This indicates that the addition of silane greatly accelerates the loss of electrons in the discharge.

The nature of this increased loss mechanism can be deduced from Fig. 5, which is the spatial variation of the electron density as a function of silane percentage obtained from Eq. (3). As silane is added to the discharge, the overall electron density goes down as shown before in Fig. 4. In addition, as the silane percentage increases, the profile becomes more uniform with r . In terms of the raw data (e.g., Fig. 3), this is indicated by a decrease in the frequency shift for both modes (reduced electron density) and a proportionately larger decrease for the TE_{111} mode, indicating that the reduction in axial electron density is larger than for that near the wall, hence the more uniform profile. This flattening is indicative of an increased volumetric loss process caused by the addition of silane. At these pressures, volumetric recombination is not likely to be a significant electron loss process, so we attribute the increased electron losses to dissociative attachment to silane or one of its dissociation products. To determine the rate coefficient for this process, the dc power supply was replaced by a pulsed supply, and the electron loss rate measured.

IV. PULSED MEASUREMENTS

The electron loss rate was determined by pulsing the hollow cathode to create a plasma, and measuring the resonant frequency shift as a function of time in the afterglow. Figure 6 is a plot of the time dependence of electron density for pure helium and for a 5% SiH_4/He mixture, both at 300 mT. The time constant for the decay in pure helium is on the

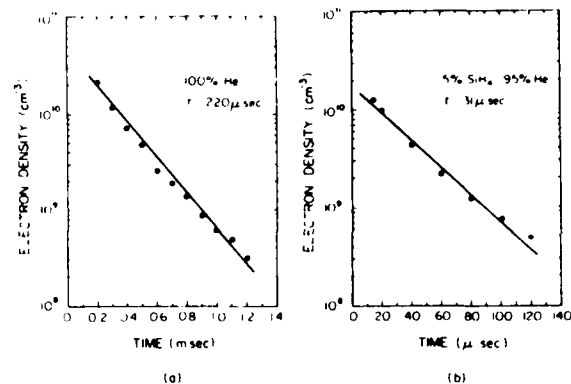


FIG. 6. Time dependence of electron density in the afterglow for 300 mT of 100% He (a) and 5% silane in helium at 300 mT (b).

order of hundreds of microseconds, characteristic of electron loss by ambipolar diffusion to the walls. When silane is added to the gas mixture, even in small amounts, there is a very noticeable increase in the rate of electron density decay. In Fig. 6, the decrease in decay time constant is over an order of magnitude for a 5% silane in helium mixture. This indicates that the addition of silane increases electron losses in the plasma; the major loss process is no longer diffusion to the walls, but is instead a volumetric loss process. Given the electronegative nature of silane and silane radicals, this volumetric loss is most likely due to negative ion formation by dissociative attachment.

The dependence of the electron decay time constant on the pulse width of the excitation is shown in Fig. 7, a plot of the electron decay time constant versus pulse width for 300 mT of a 5% SiH_4/He mixture. An increase in the pulse width applied to the discharge causes a decrease in the decay

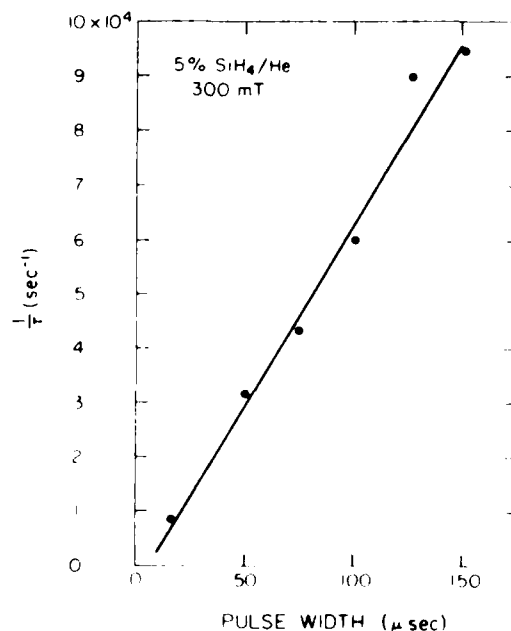


FIG. 7. Variation of the inverse time constant with pulse width for 5% silane in helium.

time constant. Similar behavior is observed when the current in the pulse is increased while holding the pulse width constant: the decay time decreases with increasing current. The effect of increasing pulse width and pulse current is to increase the dissociation of the parent SiH_4 molecules, thus reducing the SiH_4 molecule density in the plasma. Since the decay constant increases as the dissociation of SiH_4 increases, we conclude that the electron attachment is due primarily to some product specie of the dissociation of SiH_4 (SiH_x or H_2), and that attachment to SiH_4 is not significant in these experiments.

A quadrupole mass spectrometer was used to determine the relative concentration of the various dissociation products of silane. Distinct peaks were observed for H , H_2 , SiH , SiH_2 , and SiH_3 . The height of the peak corresponding to molecular hydrogen indicated that H_2 is a major dissociation product of silane in this discharge, so experiments were performed to determine whether dissociative attachment to H_2 is a factor in the large electron loss in silane discharges. The silane/helium mixture used previously was replaced by molecular hydrogen diluted in helium. The result of measurements of the reciprocal time constant versus percent H_2 show that as H_2 is added to helium, the time constant for electron decay increases, which is readily accounted for by the lower diffusion constant of H_2^+ in helium compared to He^+ .⁸ Similar experiments were performed by adding H_2 to the 5% SiH_4/He mixture, with the result that again the time constant for electron loss increased. This indicates very clearly that dissociative attachment to H_2 produced from the dissociation of SiH_4 is not a significant process in silane discharges. The mass spectroscopic measurements also showed that the peak corresponding to SiH was very small, but those for SiH_2 and SiH_3 were roughly equal in height, and over an order of magnitude higher than that for SiH . From this we conclude that the primary dissociative attachment process is to SiH_2 , SiH_3 , or possibly both.

These measurements make possible an estimate of the rate coefficient for the dissociative attachment process in this plasma. Assuming that the attachment process is fast compared to diffusion, and that recombination of electrons and positive ions is negligible at these pressures, the decay process can be described by

$$dN_e/dt = -k [\text{SiH}_x] N_e, \quad (4)$$

where k is the rate coefficient for the process and $[\text{SiH}_x]$ is the density of the attaching specie (SiH_2 or SiH_3), which gives a time constant for the process of

$$\tau = 1/k [\text{SiH}_x]. \quad (5)$$

Increasing the pulse width increases the dissociation of the parent SiH_4 molecule into SiH_2 , SiH_3 , and other dissociation products. As the pulse width is increased to large values, nearly all of the parent SiH_4 molecules become dissociated, and the electron decay time constant no longer decreases since an increase in pulse width does not create any more of the attaching specie. Figure 8 shows results of measurements similar to those of Fig. 7 except that the percentage silane in helium has been reduced to one percent or less. As the pulse width is increased (with the current and voltage held constant), the inverse decay time constant initially increases, but

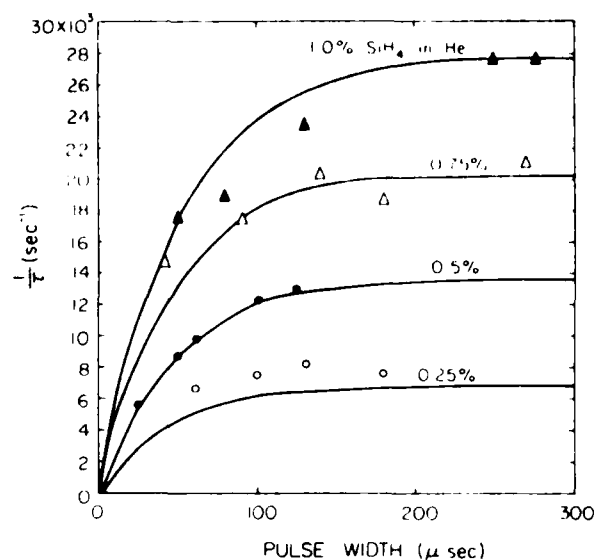


FIG. 8. Inverse time constant as a function of pulse width and percent silane in helium for small silane percentages.

then levels off and remains constant as the pulse width becomes large enough to dissociate most of the parent SiH_4 molecules. The $1/\tau$ for 0.25% silane is slightly higher than expected, which is attributed to the fact that at this low percentage, the decay rate of the electron density due to attachment becomes comparable to that for diffusion to the walls, so both processes contribute to the measured decay. When the pulse width is large enough to dissociate all of the silane, it is possible to obtain an estimate for k . The density of the SiH_4 parent molecule is known from the pressure and the percent silane in the gas mixture. Using the assumption that for large pulse widths, all of the parent silane molecules are dissociated in the discharge into an attaching specie (so $[\text{SiH}_x]$ equals the input silane density), k can be determined by dividing the reciprocal time constant by the silane density. Using the large pulse width values of $1/\tau$ from Fig. 8, we estimate a rate coefficient for this process of $2.65 \pm 0.19 \times 10^{-10} \text{ cm}^3/\text{sec}$. Since the density of attaching species is likely to be somewhat smaller than the input silane density, the estimate obtained is a lower bound on the real value of k .

V. CONCLUSION

In conclusion, a pulsed hollow cathode discharge has been used to investigate the time dependence of the electron density in SiH_4/He deposition plasmas. Addition of silane greatly decreases the electron decay time constant due to volumetric attachment of electrons. Varying the pulse width and current show that the attachment is due mainly to a product of the dissociation of silane, and is not due to SiH_4 itself. Further measurements show that H_2 is not the major attaching specie. Thus, we conclude that attachment is an extremely important process in silane discharges, and most likely proceeds through the silane dissociation products SiH_2 and SiH_3 .

¹I. Haller, Appl. Phys. Lett. 37, 282 (1980).

²M. S. Gordon, Chem. Phys. Lett. 59, 410 (1978).

³G. Turban, Y. Catherine, and B. Grolleau, Thin Solid Films 67, 309 (1980).

⁴G. Turban, Y. Catherine, and B. Grolleau, Plasma Chem. Plasma Processing 2, 61 (1982).

⁵J. Perrin, A. Lloret, G. de Rosny, and J. P. M. Schmitt, Int. J. Mass Spectrosc. Ion Processes 57, 249 (1984).

⁶A. Garscadden, in *Proceedings of the 6th International Symposium on Plasma Chemistry*, edited by M. I. Boulos and R. J. Munz (McGill Univ., Montreal, 1983) 388.

⁷A. Gilardini, *Low Energy Electron Collisions in Gases* (Wiley, New York, 1972).

⁸H. S. W. Massey, *Electronic and Ionic Impact Phenomenon* (Oxford, London, 1971).

SECTION IV

THE SPATIAL AND TEMPORAL EVOLUTION
OF THE GLOW IN A RF DISCHARGE

by

G. A. Hebner
J. T. Verdeyen

The Spatial and Temporal Evolution of the Glow in an RF Discharge

G. A. HEBNER AND J. T. VERDEYEN, SENIOR MEMBER, IEEE

Abstract—The temporal and spatial evolution of the glow in a 1.0- and 2.6-MHz radio-frequency (RF) excited discharge has been photographed with a high-speed framing camera. Evidence is presented showing electrons with a ballistic behavior in the body of the glow and a time delay between the maximum optical intensity of the glow and the maximum RF voltage. The effect of the dc self-bias on the glow is also shown. The implications of these observations on the dynamics of the ion motion in the plasma are discussed.

I. INTRODUCTION

RADIO-FREQUENCY (RF) plasma etching and deposition of semiconductor materials has found increasing use in industry [1], [2]. However, the basic dynamics of the RF plasma are not completely understood. Thus in recent years there has been increasing interest in studying the fundamental dynamics of the RF plasma in etching, deposition, and noble gases.

Early studies of the RF plasma have examined the formation and characteristics of the sheaths [3], the energy distribution of the ions striking the cathode [4], and the plasma potential [5], [6] in helium, neon, and argon. More recent studies have focused on the temporal and spatial evolution of the plasma. Several techniques such as Langmuir probes to observe electron properties [7], [8], optical emission actinometry to estimate relative radical concentrations [9]–[11], time-resolved LIF to observe ion concentrations and motion [12], and field-induced state mixing to measure electric fields and potentials [13] have proven useful. All of these studies have helped to increase the understanding of RF plasmas and to develop useful models [1], [4], [6], [14].

Thus in order to understand the dynamics of the RF discharge, it is important to observe both the temporal and spatial evolution of the plasma. To achieve this, we have used a framing camera to photograph the evolution of a helium plasma. The use of the framing camera allows one to observe the effect of bias, power, and pressure on the development of the entire plasma. In order to isolate a single spectral line, an interference filter was used for some photographs to observe the 5875-Å ($3^1D \rightarrow 2^1P$) line of helium. The lifetime of this state, 14 ns [15], is

relatively short compared to the RF period (400 ns and 1 μ s). By using the framing camera, we have observed evidence of electrons with a ballistic behavior in the body of the glow and a time delay between maximum light from the glow and the maximum RF voltage.

II. EXPERIMENTAL APPARATUS

The parallel-plate RF circuit and the camera system are shown in Fig. 1. The RF system consists of a parallel-plate discharge tube, matching network, and power supply. Two matching networks are available at 1.0 and 2.6 MHz. The aluminum electrodes are 10 cm in diameter and 3 cm thick and are mounted in a Pyrex tube. Electrode separation is 3.8 cm. The rear side of the driven electrode is separated from a ground plane by a 1.5-mm-thick Teflon sheet to confine the discharge to only one side of the driven electrode. Helium flows through the system at pressures of 300 mT to 1 T.

The applied RF voltage is monitored by a calibrated capacitance voltage divider and the current is monitored with a Tektronix current probe. Voltage and current waveforms (Fig. 2) are digitized and multiplied by a computer to obtain the instantaneous power. The power becomes negative during portions of the RF cycle since the discharge is reactive. The power peaks at the same time that the current reaches a maximum. However, the voltage peaks after the current and the maximum light output peaks after the voltage peak (see Figs. 5–7). These points will be discussed in detail later. The dc self bias is measured through a 200 mH choke to filter the RF components of the voltage. Bias voltages are generally in the range of 0 to -120 V with short-circuit currents of 0.9 mA. Operating power levels are 2–20 W into the plasma.

The high speed camera consists of a standard camera lens (50 mm, f2), a gated image intensifier tube, and a conventional oscilloscope camera to collect and record the image. When used, the 5875-Å interference filter is mounted in front of the lens. To synchronize the camera to the RF period, the RF signal from the capacitance voltage divider is divided digitally to approximately 400 Hz. This signal triggers a digital delay generator, which is used to vary the position of the trigger of the high-voltage pulser over the RF cycle. The high-voltage pulses have a 25-ns width and an 800-V amplitude with less than 10 ns of jitter. Since the voltage across the microchannel plate determines the gain of the tube, the voltage pulse creates

Manuscript received June 28, 1985; revised August 26, 1985. This work was supported by the Army Research Office under Contract DAAG 20-83-K-0108 and by the Aero Propulsion Laboratory, USAF, under Contract F33615-83-K-2335.

The authors are with the Department of Electrical and Computer Engineering, University of Illinois at Urbana-Champaign, Urbana, IL 61801.
IEEE Log Number 8046830.

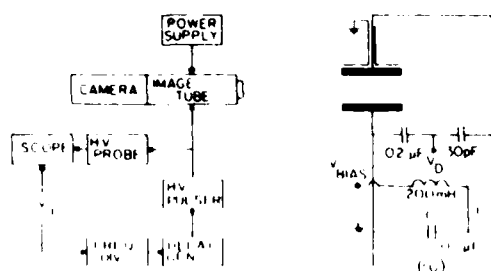


Fig. 1. Schematic diagram of the framing camera system and the RF discharge circuit. The camera is 80 cm from the plasma. Component values are $L = 28 \mu\text{H}$, $C = 200 \text{ pF}$ for 2.6-MHz operation, and $L = 400 \mu\text{H}$, $C = 700 \text{ pF}$ for 1.0 MHz.

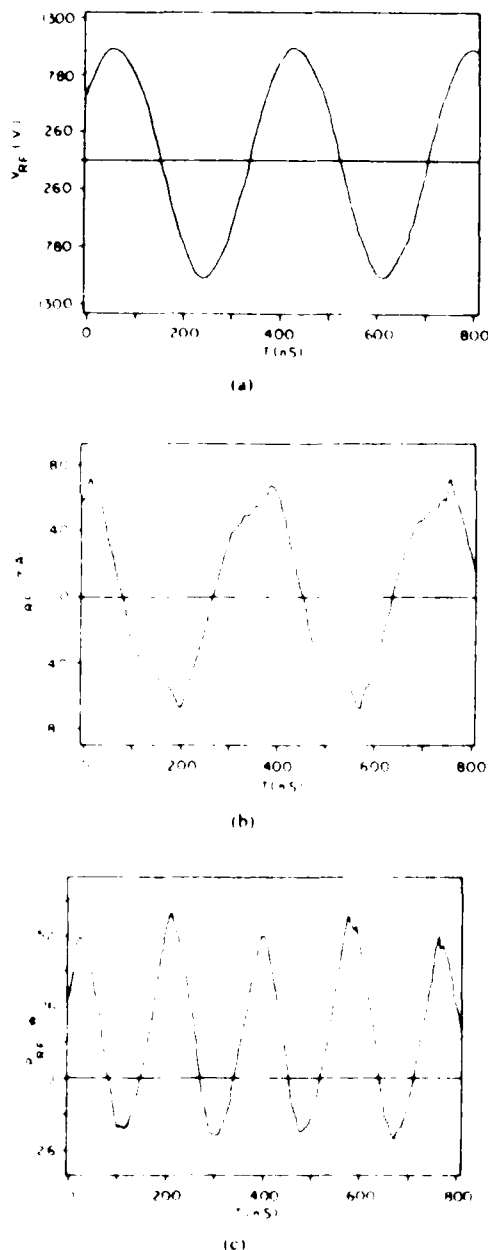


Fig. 2. Typical waveforms for the discharge circuit: (a) voltage, (b) current, and (c) power. The operating conditions were 500 mT of helium, 22 V dc self-bias, and 10 W into the plasma.

a very fast shutter, as well as amplifying the available light. By observing both the RF discharge voltage and the high-voltage pulse applied to the image tube, the portion of the RF cycle that is being photographed can be determined and adjusted with the delay generator. The images are recorded on 400 ASA Tri-X. The negatives are analyzed with a microdensitometer to determine the optical density through the middle of the discharge.

III. RESULTS AND DISCUSSION

Two representative framing photographs of the RF plasma are shown in Fig. 3. The T above one of the electrodes marks the driven electrode, while the unmarked electrode is grounded. The electrode locations are marked by the white bands. In Fig. 3(a), the driven electrode is the cathode. Note the well-defined cathode-sheath region and the way the light intensity decreases towards the anode. The discharge does not fill the entire volume between the electrodes, but instead tends to form a truncated cone with the base at the cathode. In Fig. 3(b), the unmarked plate is now the cathode and the marked plate is the anode. Again, the glow has a well-defined sheath with the light intensity decreasing towards the anode in a truncated cone. This general shape was common to all the photographs.

The cone shape has several possible origins. The first is that the discharge volume is circular. The second is that the ion spatial distribution is nonuniform due to diffusion. As a result, the electrons produced by ion bombardment of the cathode should have a distribution that peaks in the center of the discharge and decreases radially. Furthermore, the field due to the wall sheaths tends to deflect the electrons towards the center of the glow. Due to the difficulty in isolating all the possible causes, no attempt was made in this study to identify the dominant mechanism.

The shape of the glow in Fig. 3 appears to be similar to the shape of the negative glow in a parallel-plate dc discharge. It has been hypothesized that the RF discharge is similar to a hollow cathode discharge with alternating cathode dark spaces and a common negative glow [1]. If this is the case, then the electrons from the cathode will have a ballistic component. An object placed in the electron beam should cast a shadow since the electrons that are accelerated from the cathode are intercepted by the object and are removed from the downstream discharge process. The electrons below the object, which are left from the previous half cycle, experience insufficient field to accelerate and produce a glow. Consequently, the region downstream from the obstacle will be relatively dark. Those electrons that do not strike the object should continue relatively straight towards the anode and not be affected by the obstruction. Thus the glow from the cathode to the object will be similar to the glow without the object. However, there should be an abrupt decrease in optical emission below the object creating a shadow effect.

To test the theory that the excitation results from those electrons that have a ballistic component, a quartz slide ($2.5 \times 8 \times 1 \text{ mm}$) resting on three small quartz legs was

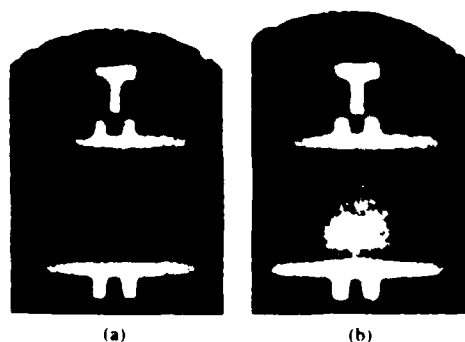


Fig. 3. Framing camera photographs of the 5875 Å glow at two times of the RF period. The driven plate is marked with a T. In (a) the driven electrode is at the maximum negative voltage. For (b) the driven electrode is at the maximum positive voltage. The intensity difference is due to the printing process. Discharge conditions are 500-mT helium, 4.5 W into the plasma, RF voltage 350 V_{peak}, and 1.0 MHz. Electrode separation is 6.1 cm.

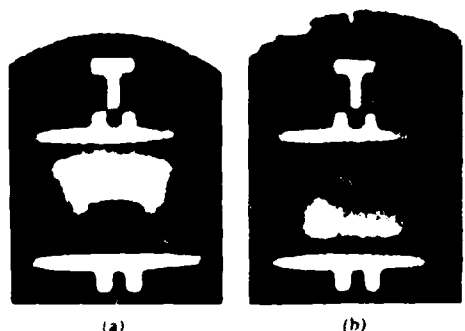


Fig. 4. Framing camera photographs of the 5875 Å glow with a quartz slide in the middle of the discharge. In (a) the driven electrode is at maximum negative voltage while (b) is at maximum positive voltage. Discharge conditions are the same as Fig. 3.

inserted into the middle of the discharge. The photographs are shown in Fig. 4. In Fig. 4(a), the driven electrode is the cathode. Note the very distinct vertical shadow cast below the slide. The opposite half-cycle is shown in Fig. 4(b). As expected, the shadow now extends up to the driven electrode which is the anode. Except for the dark space on the anode side of the slide, the glow with and without the slide (Fig. 3) does not appear to be significantly different. In addition, the relatively straight sides of the dark space indicate that the electrons that do not intercept the slide continue relatively straight towards the anode, and the dark space implies that the electric field in the dark space is insufficient to accelerate electrons to produce a glow. Thus these distinct shadows tend to indicate that the body of the glow is produced by a beam of electrons which is consistent with the previous simple model of the RF plasma.

However, this simple model must be expanded in the RF plasma to include the dynamics of the ion motion since the time required for an ion to traverse the sheath is significant when compared to the RF period. Because the electrons that produce the glow are the result of both ion bombardment of the cathode and electron ionization and

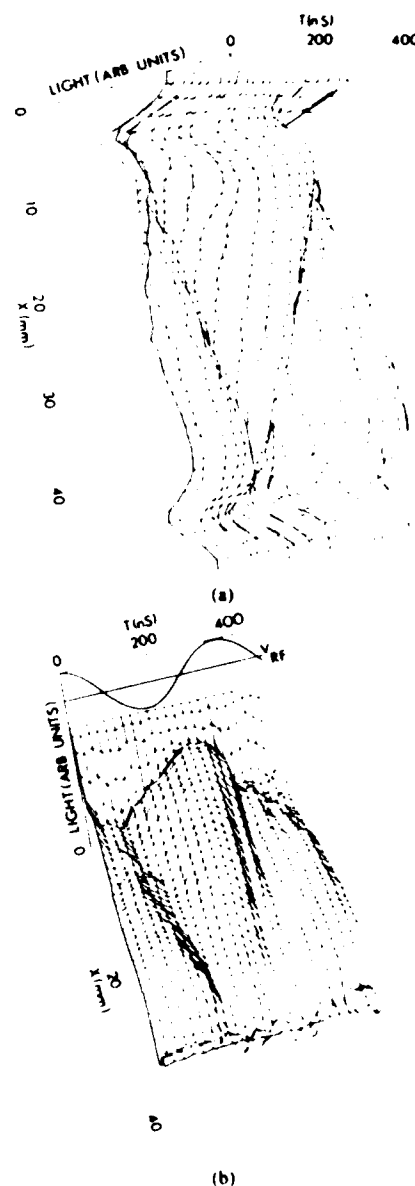


Fig. 5. Three-dimensional plots of the evolution of the glow in a parallel plate RF system. The voltage reference is shown in (b). Conditions are 500 V_{peak}, 1-T helium, -20 V self-bias, 4 W into the plasma, and 2.6 MHz. Electrode separation is 4.1 cm. All optical lines are photographed.

multiplication in the sheath, the transit time of an ion across the sheath will affect the temporal evolution of the glow. To address the question of ion motion affecting the glow, microdensitometer scans of the negatives are used to construct a three-dimensional picture of the plasma emission. The results of one of these scans is shown in Fig. 5. The microdensitometer is scanned from the driven electrode to the grounded electrode through the middle of the discharge. Proper spatial alignment is ensured by the reference marks on the electrode bands which also serve as a constant intensity reference point for comparison of photographs. The lines at $x = 0$ mm and $x = 46$ mm represent the reflected light from the reference bands. Due

to a slight defocusing and the resolution of the microdensitometer, the driven electrode edge is located at $x = 2.5$ mm while the grounded electrode is at $x = 43.5$ mm. The fast slope down from the reference bands provides a measure of the microdensitometer spatial resolution. To allow a comparison between the applied voltage and the light intensity, the RF voltage applied to the driven electrode is shown in Fig. 5(b).

One can observe in Fig. 5 that the light peaks after the voltage maximum. In addition, the glow continues to grow over the entire cathode cycle of the electrode. The growth of the glow and the relative delay between the maximum voltage and light can be attributed to the transit time of ions across the sheath and the presence of relatively long lifetime states in the following way. At low potentials, the electrons produced by ion bombardment of the cathode will have relatively low energy. Consequently, they will make only a few ionizing and exciting collisions before their energy is reduced to a low value. Since the electrons are unable to penetrate very far into the gas, the glow will initially be relatively close to the cathode. As the potential increases, the energy and number of electrons will increase. As a result, the electrons will penetrate farther into the gas and the peak of the glow will move away from the cathode. The movement of the glow peak away from the cathode is observed in Fig. 5(a) between the times of $100 \text{ ns} < t < 140 \text{ ns}$ and $260 \text{ ns} < t < 300 \text{ ns}$. The different starting times for the growth of the glow are due to the effect of the dc self-bias. When the voltage waveform in Fig. 5(b) is offset by the bias voltage, the growth of the glow begins at approximately the same time after a zero-voltage crossing. At still higher potentials, the energy and number of the electrons crossing the sheath continues to increase. The electrons now have sufficient energy to cause ionization and excitation in the sheath and the maximum in light intensity begins to move towards the cathode, as shown in Fig. 5(a). At the maximum cathode potential, large numbers of ions are created which take time to drift across the sheath. Thus the maximum in light, which is the result of electrons produced by ion bombardment of the cathode, will be delayed with respect to the voltage. As the potential decreases, the number of ions and the number and energy of electrons decreases and the glow intensity decreases. The decay of the light after this point is due to the relatively long lifetimes of strong emission lines such as the 5015 \AA line ($\tau = 75 \text{ ns}$) [15] and the cascading of higher energy, long-lifetime states.

The movement of the 5875 \AA glow near the electrodes at 1.0 MHz is shown in Fig. 6. The reference points used for these measurements are described in Fig. 6(a). Briefly, L is the distance from the electrode edge to the intercept of the curve determined by the microdensitometer resolution and the increase of the light due to the discharge. This intercept is a convenient measure of the intensity of the glow near the electrode since the exact location of the peak excitation is difficult to locate.

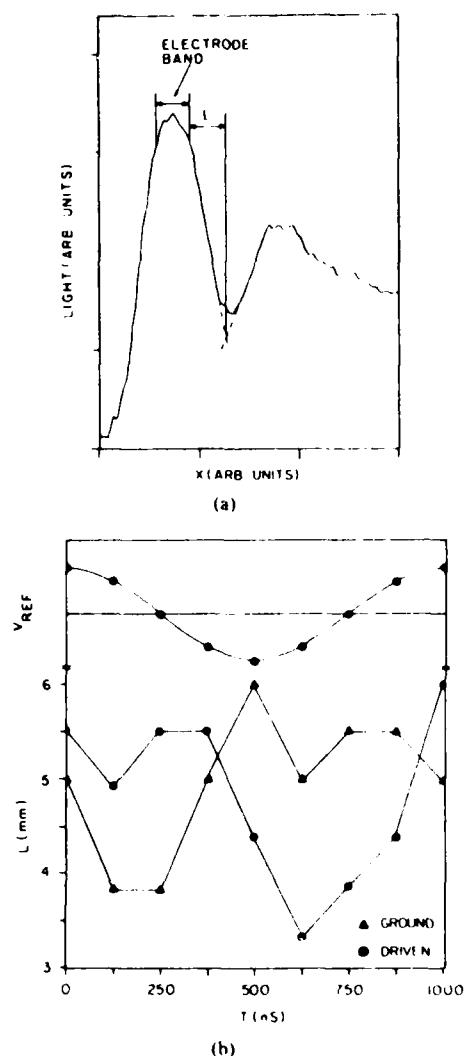


Fig. 6. Movement of the 5875 \AA glow near the driven and ground electrodes. (a) shows a portion of a microdensitometer scan of a negative. The location of the band describing the electrode is as marked. L is the distance from the electrode edge to the intercept of the extrapolated lines determined by the microdensitometer resolution and the increase in the glow. (b) shows the evolution of the glow near the driven (\bullet) and the ground (Δ) electrodes. The voltage applied to the driven electrode is as shown (arbitrary units). The discharge conditions are the same as Fig. 5.

Many of the features of Fig. 5 are also observable in Fig. 6. As the driven electrode becomes more negative, the glow increases in intensity and moves towards the cathode as previously observed. Later, the glow at the ground electrode begins to grow as the electrons penetrate the gas from the cathode. At the maximum voltage, many ions are formed, and since these ions take time to drift across the sheath, the glow continues to increase at the cathode and anode as observed in Fig. 5. As the potential goes to zero, both glows move away from their respective electrode since the number and energy of the electrons is reduced. This is in contrast to Fig. 5, where the glow continues into the next half-cycle due to long-lifetime states. However, both Figs. 5 and 6 display the basic

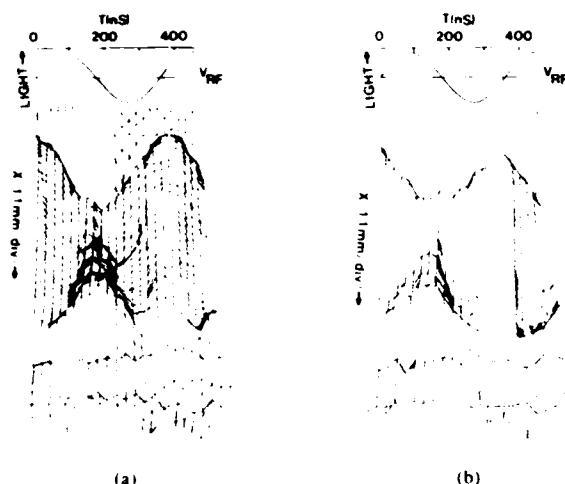


Fig. 7. Three dimensional plots of the evolution of the 5875 Å glow in a parallel plate system showing the effect of the dc self bias on the glow: (a) is biased at -20 V while (b) is shorted to ground (0.9 mA short-circuit current). The voltage reference is as shown. The driven electrode is located at $x = 2$ mm while the ground electrode is at $x = 54$ mm. Discharge conditions are 500 V_{peak}, 1-T helium, 5 W into the plasma, 2.6 MHz, and 5.2 cm plate separation for both figures. The light intensity is in arbitrary units.

property of the voltage maximum leading the maximum light intensity of the glow.

The effect of the dc self-bias on the driven electrode at 2.6 MHz can be observed in Fig. 7. With the bias present (Fig. 7(a)), the 5875-Å glow next to the driven electrode when it is the cathode is much wider and brighter than the glow that forms when the ground plate is the cathode. In addition, the glow extends further towards the anode when the driven electrode is negative. If the bias is shorted to ground (Fig. 7(b)), the shape of the glow at the driven and ground electrodes is approximately the same.

There are two possible explanations for the enhancement of the glow when the dc bias is present and the driven electrode is the cathode. The first is that the driven plate is negative longer than it is positive as a result of the negative bias. This allows the creation of additional electrons due to a longer period of ion bombardment of the cathode. The second possible explanation is that there may be an increase of the electric field at the driven electrode due to a difference in the ratio of cathode area to effective ground area when the driven electrode is a cathode as compared to when the ground electrode is the cathode [1], [5]. In practice, the enhancement of the glow when the driven electrode is a cathode is probably the result of a combination of these two effects. However, the increase of the glow due to electric field enhancement at the driven plate is thought to be minimized in our system since the electrodes are mounted in a Pyrex tube with little surrounding material.

IV. CONCLUSION

In order to understand the dynamics of the RF plasma, it is important to study both the temporal and spatial evolution of the plasma. The framing camera, which provides spatial and temporal resolution, as well as spectral sensitivity, has allowed the observation and measurement of the growth of the glow and the effect of the dc self-bias on the shape of the glow. We have noted that the body of the glow appears to be excited by a beam of electrons with a ballistic component produced by ion bombardment of the cathode and that the shadow is consistent with the theory that the body of the plasma is similar to a negative glow. The photographs also show that the maximum light from the glow follows the peak cathode voltage and the current and power maximum. Due to the delay in the glow peak, the ion transit time across the sheath appears to be an important factor in the dynamics of the glow.

REFERENCES

- [1] B. Chapman, *Glow Discharge Processes*. New York: Wiley, 1980, ch. 5.
- [2] D. L. Flamm, V. M. Donnelly, and D. E. Ibbotson, "Basic chemistry and mechanisms of plasma etching," *J. Vac. Sci. Technol. B*, vol. 1, pp. 23-30, 1983.
- [3] H. S. Butler and G. S. Kino, "Plasma sheath formation by radio-frequency fields," *Phys. Fluids*, vol. 6, pp. 1346-1355, 1963.
- [4] W. D. Davis and T. A. Vandershice, "Ion energies at the cathode of a glow discharge," *Phys. Rev.*, vol. 131, pp. 219-228, 1963.
- [5] J. W. Coburn and E. Kay, "Positive ion bombardment of substrates in rf diode glow discharge sputtering," *J. Appl. Phys.*, vol. 43, pp. 4965-4971, 1972.
- [6] K. Kohler, J. W. Coburn, D. E. Hone, E. Kay, and J. H. Keller, "Plasma potentials of 13.56 MHz rf argon glow discharges in a planar system," *J. Appl. Phys.*, vol. 51, pp. 59-66, 1985.
- [7] R. R. J. Gange and A. Cantin, "Investigation of an rf plasma with symmetrical and asymmetrical electrostatic probes," *J. Appl. Phys.*, vol. 43, pp. 2639-2647, 1972.
- [8] M. J. Kushner, "A kinetic study of the plasma etching process. 2. Probe measurements of electron properties in an rf plasma etching reactor," *J. Appl. Phys.*, vol. 53, pp. 2939-2946, 1982.
- [9] J. W. Coburn and M. Chen, "Optical emission spectroscopy of reactive plasmas: A method for correlating emission intensities to reactive particle density," *J. Appl. Phys.*, vol. 51, pp. 3134-3136, 1980.
- [10] R. A. Gottscho and V. M. Donnelly, "Optical emission actinometry and spectral line shapes in rf glow discharges," *J. Appl. Phys.*, vol. 56, pp. 245-250, 1984.
- [11] R. d'Agostino, F. Cramarossa, V. Colaprico, and R. d'Ettole, "Mechanisms of etching and polymerization in radiofrequency discharges of CF_4-H_2 , $CF_4-C_2F_4$, $C_2F_4-H_2$, $C_3F_8-H_2$," *J. Appl. Phys.*, vol. 54, pp. 1284-1288, 1983.
- [12] R. A. Gottscho, R. H. Burton, D. L. Flamm, V. M. Donnelly, and G. P. Davis, "Ion dynamics of rf plasmas and plasma sheaths: A time resolved spectroscopic study," *J. Appl. Phys.*, vol. 55, pp. 2707-2714, 1984.
- [13] C. A. Moore, G. P. Davis, and R. A. Gottscho, "Sensitive, nonintrusive, in situ measurement of temporally and spatially resolved plasma electric fields," *Phys. Rev. Lett.*, vol. 52, pp. 538-541, 1984.
- [14] M. J. Kushner, "A kinetic study of the plasma etching process. 1. A model for the etching of Si and SiO_2 in C_4F_8/H_2 and C_4F_8/O_2 plasmas," *J. Appl. Phys.*, vol. 53, pp. 2923-2938, 1982.
- [15] W. L. Wiese, M. W. Smith, and B. M. Glennon, *Atomic Transition Probabilities*, vol. 1. Washington, DC: U.S. Dep. of Commerce, NBS, 1966, pp. 9-15.

SECTION V

ENHANCEMENT OF THE PLASMA DENSITY AND DEPOSITION RATE
IN RF DISCHARGES

by

L. J. Overzet
J. T. Verdeyen

Enhancement of the plasma density and deposition rate in rf discharges

L. J. Overzet and J. T. Verdeyen

Department of Electrical and Computer Engineering, University of Illinois at Urbana-Champaign, 1406 West Green Street, Urbana, Illinois 61801

(Received 6 December 1985; accepted for publication 20 January 1986)

The peak and time averaged electron density in rf excited silane-helium mixtures increased significantly above the cw value by square wave modulating the source. The deposition rate of amorphous hydrogenated silicon films is also enhanced and apparently follows the electron density. Attachment to the discharge products appears to be responsible.

The properties of rf glow discharges in silane and helium, as well as the materials deposited from these discharges, have been the focus of extensive research.¹⁻¹² One of the major impetus for research on the deposition kinetics of amorphous hydrogenated silicon has been the desire to produce high quality films at enhanced deposition rates. We have uncovered a process which enhances deposition in low power rf discharges significantly. Both the deposition rate and the time averaged electron density have been enhanced by square wave amplitude modulating (SQWM) the excitation of the silane-helium mixture (i.e., 100% modulation depth and 50% duty cycle). Even though this work has concerned deposition, the data suggest that this phenomenon may be found in other attaching gases including those used for etching.

The experimental apparatus in Fig. 1 is conventional in its essential features excepting perhaps our use of 2.9 rather than 13.56 MHz. Power is coupled capacitively to the glow through the matching network shown in the upper section and the incident/reflected values are measured with a Bird wattmeter. An MKS 254A flow controller determines and monitors the flow of gas through the plasma volume and also controls the fractional silane content of the total. Typical flows are in the range of 30 sccm for pressures on the order of 0.6 Torr of 0.5% SiH₄ in helium.

A double pass microwave bridge circuit, shown below the discharge section in Fig. 1, is used to measure the electron density within the 9 cm diameter \times 5 cm discharge volume. The microwave circuit involves a standard measurement technique which has been discussed extensively in the literature.^{13,14} Only the general idea is stressed here; namely, the change in the detector output is directly proportional to the electron density. Electron densities greater than 10^6 cm⁻³ were measurable using this circuit at a microwave frequency of 8.558 GHz.

The electron density is emphasized because of its microscopic nature within the glow discharge and because it yields information on a time scale which is short compared to most kinetic reactions. By way of comparison, the macroscopic growth rate or film quality are integrations over large time periods of complex and often competing processes. Despite this difference in the nature of these observables, we have found that the deposition rate follows the dependence of the time averaged electron density, in agreement with Turban^{2,3} and Kampas.⁹

The time evolution of the electron density in helium and

a 0.5% silane mixture in response to a SQWM excitation (100% modulation depth and 50% duty cycle) is compared in Fig. 2 to that of a cw discharge at the same peak power (and consequently twice the average power). The results for a helium discharge, shown in Fig. 2(a), follow intuitive logic. The square wave modulated source produces an essentially square wave modulated electron density, and the identical peak power to the discharge produces the same peak electron density. Obviously, the decreased average power to the SQWM glow produces a corresponding decrease (by a factor of 2) in the time averaged electron density.

The electron density in a 0.5% silane mixture does not follow this intuitive logic as is illustrated in Fig. 2(b). The time dependence of the electron density in the SQWM glow is no longer nearly square wave in shape, and despite having the same peak power, the instantaneous electron density is radically different from the cw value. Indeed, Fig. 2(b) shows that the electron density has a rather complex and contorted time behavior, and has not reached the cw equilib-

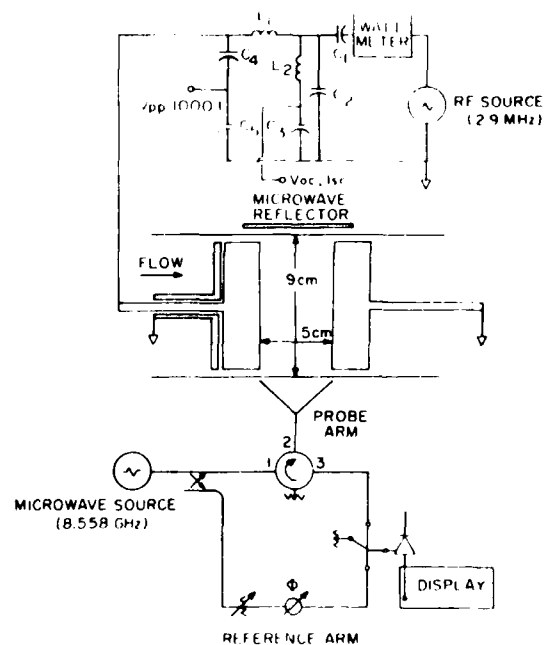


FIG. 1 rf matching network (upper), plasma region (center), and microwave bridge circuit (lower)

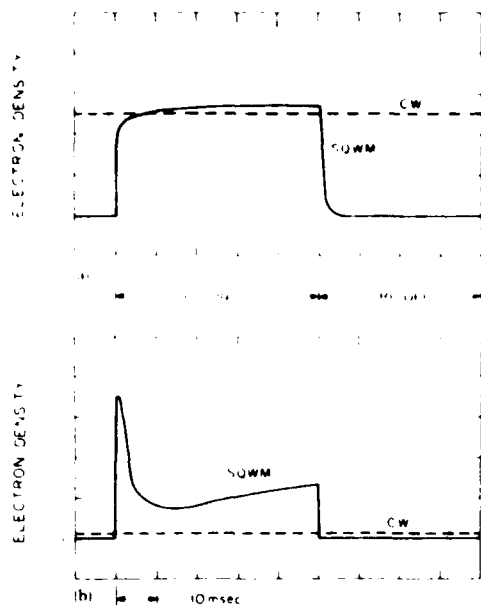


FIG. 2. Time dependence of the electron density for a square wave modulated excitation source (SQWM) (100% modulation depth and 50% duty cycle) and a continuous wave source (cw) in (a) helium and (b) 0.5% silane in helium.

rium value even in the 50 ms on time. Consequently, the density averaged over the period of modulation is considerably larger for the SQWM excitation as can be deduced from Fig. 2(b).

The dependence of the electron density on the modulation frequency is shown in Fig. 3. For a constant peak power of 18 W, the time averaged electron density can be enhanced by as much as a factor of 2–3 in the SQWM glow. For low (< 5 Hz) and for high (> 5 kHz) modulation frequencies, the time averaged electron density in the SQWM glow approaches the expected 1/2 of the cw value. The film thickness (for a 15-min deposition time) is shown in Fig. 4 along

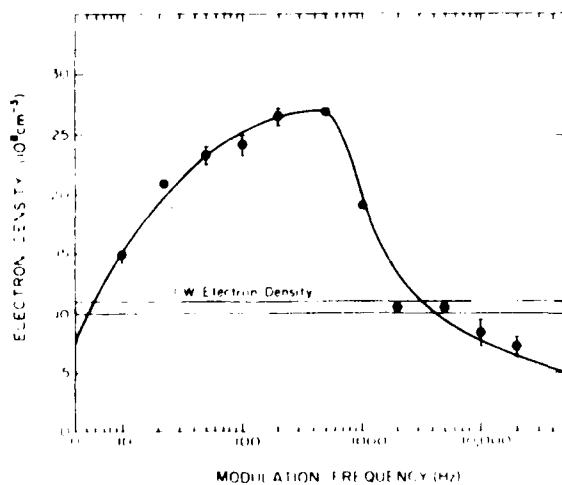


FIG. 3. Dependence of the time averaged electron density on the square wave modulation frequency in a 1% silane discharge (0.6 Torr). The peak power is ~18 W.

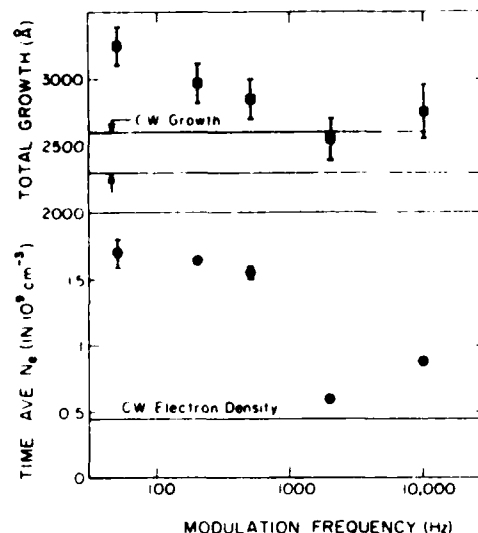


FIG. 4. Total film thickness after 15 min and time averaged electron density during the growth as a function of the modulation frequency. The peak power varied between the data points, but remained in the 15–18 W range. All discharges were 1% silane in helium at approximately 0.6 Torr.

with the time averaged electron density during the growth. These films were grown on quartz substrates placed on the driven electrode (in Fig. 1) and the film thickness was measured with a Dektak profilometer. Note that the data points shown in Fig. 4 were *not* all taken at the same peak power and thus the densities shown in Figs. 3 and 4 cannot be compared; however, the correlation between electron density and deposition in Fig. 4 is significant. The deposition rate can be seen there to follow the magnitude of the electron density.

Both the contorted time evolution shown in Fig. 2 and the enhancement of the time averaged electron density in Fig. 3 indicate a complex interrelationship between the electron density, ion density, and the depositing species. While the exact electron-ion kinetics are not clear from the data presented in Figs. 2 and 3, one may speculate based upon these data. In Fig. 2(b), the electron density increases to a high value initially and then decreases to a quasi-equilibrium value. This time dependence is consistent with the results of Fleddermann *et al.*⁴ who demonstrated that the products of silane dissociation attached electrons faster than silane itself. These products are not within the discharge when it is first turned on; therefore the electron density rises quickly. As the discharge proceeds, however, silane is dissociated into these attaching products, and attachment produces the rapid decay of the electron density after its initial rise. Unfortunately, the secondary increase of electron density [in Fig. 2(b)] and the approach to the cw value are not understood at this time.

The fact that the deposition rate increases in the SQWM discharge even though the time averaged power is halved may indicate that the products—possibly even the negative ions—of the initial silane dissociation are involved in deposition. These negative ions are confined by the sheaths in the same manner as are electrons in the cw glow. Hence the enhanced growth rate in the SQWM glow may be partially

due to deposition by the negatively charged radicals in the afterglow when such sheaths are greatly reduced. This speculation regarding the enhancement remains to be proven.

Even though the detailed processes are not known at the present time, it is surely true that the enhanced electron density in the SQWM glow permits an increase in the neutral and ionic products along with an enhanced deposition rate. Similar effects may be found in etching discharges; indeed, there may be a hint of this in a recent paper.¹⁵ The authors have also observed a similar (although somewhat less pronounced) enhancement in the electron density in a CF_4 glow.

This work was supported by the U.S. Air Force Aeronautical Systems Division (AFSC) Wright-Patterson Air Force Base.

¹⁵J. C. Knights, R. A. Lujan, M. P. Rosenblum, R. A. Street, D. K. Biegelsen, and J. A. Reimer, *Appl. Phys. Lett.* **38**, 331 (1981).

- ²G. Turban, Y. Catherine, and G. Grolleau, *Thin Solid Films* **60**, 147 (1979).
- ³G. Turban, Y. Catherine, and G. Grolleau, *Plasma Chem. Plasma Process.* **1**, 61 (1982).
- ⁴C. B. Fleddermann, J. H. Beherman, and J. T. Verdeyen, *J. Appl. Phys.* **58**, 1344 (1985).
- ⁵H. F. Sterling and R. C. G. Swann, *Solid State Electron.* **8**, 653 (1965).
- ⁶W. E. Spear and P. G. LeComber, *Solid State Commun.* **17**, 1193 (1975).
- ⁷B. A. Scott, M. H. Brodsky, D. C. Green, P. B. Kirby, R. M. Plecenik, and E. E. Simonyi, *Appl. Phys. Lett.* **37**, 725 (1980).
- ⁸F. J. Kampas and R. W. Griffith, *Appl. Phys. Lett.* **39**, 407 (1981).
- ⁹F. J. Kampas, *J. Appl. Phys.* **54**, 2276 (1983).
- ¹⁰J. C. Knights, *Jpn. J. Appl. Phys. Suppl.* **18-1**, 101 (1979).
- ¹¹R. A. Street, J. C. Knights, and D. K. Biegelsen, *Phys. Rev. B* **18**, 1880 (1980).
- ¹²A. Garscadden, G. L. Duke, and W. F. Bailey, *Appl. Phys. Lett.* **43**, 1012 (1983).
- ¹³A. L. Gillardini, *Low Energy Electron Collisions in Gases*, 1st ed. (Wiley, New York, 1972), pp. 236-254.
- ¹⁴A. K. Bhattacharya, J. T. Verdeyen, F. T. Adler, and L. Goldstein, *J. Appl. Phys.* **38**, 527 (1967).
- ¹⁵R. W. Boswell and D. Henry, *Appl. Phys. Lett.* **47**, 1095 (1985).

END

10-87

DTIC